

activity (Fig. 3B). Mutation of Phe155 to alanine severely impaired crRNA processing, suggesting that this residue also plays an important role in substrate orientation. However, none of the above mutations severely disrupted crRNA binding, as judged by means of electrophoretic mobility shift assays, indicating that the structural integrity of the mutant proteins was not compromised (fig. S8). Thus, interaction between Csy4 and the closing base pair of the RNA stem is critical for pre-crRNA processing, whereas sequence-specific recognition of the penultimate base pair in the stem is less important. Incubation of Csy4 with a panel of short RNA oligonucleotides containing a variety of mutations in the CRISPR repeat stem-loop sequence further confirmed that Csy4 requires a C-G base pair closing the RNA stem and that Csy4 can accommodate different nucleotides at the penultimate RNA base pair (fig. S10).

Phylogenetic analysis of CRISPR loci suggests that CRISPR repeat sequences and structures have co-evolved with the Cas genes (19). The similarity of Csy4 at the fold level to the CRISPR-processing endonucleases CasE and Cas6 suggests that collectively they are likely to have descended from a single ancestral endoribonuclease enzyme that has diverged throughout evolution. The structure described here reveals how Csy4 and related endonucleases from the same CRISPR/Cas subfamily use an exquisite recognition mechanism to discriminate crRNA substrates from other cellular RNAs. This illustrates the importance of co-evolution in shaping molec-

ular recognition mechanisms in the CRISPR pathway. Furthermore, the ability of Csy4 to form a tight complex with the cleaved crRNA product points to Csy4 having a functional role within the CRISPR pathway that extends beyond pre-crRNA cleavage.

References and Notes

- S. J. Brouns *et al.*, *Science* **321**, 960 (2008).
- J. Carte, R. Wang, H. Li, R. M. Terns, M. P. Terns, *Genes Dev.* **22**, 3489 (2008).
- D. H. Haft, J. Selengut, E. F. Mongodin, K. E. Nelson, *PLOS Comput. Biol.* **1**, e60 (2005).
- C. R. Hale *et al.*, *Cell* **139**, 945 (2009).
- K. S. Makarova, N. V. Grishin, S. A. Shabalina, Y. I. Wolf, E. V. Koonin, *Biol. Direct* **1**, 7 (2001).
- R. Barrangou *et al.*, *Science* **315**, 1709 (2007).
- L. A. Marraffini, E. J. Sontheimer, *Science* **322**, 1843 (2008).
- L. A. Marraffini, E. J. Sontheimer, *Nat. Rev. Genet.* **11**, 181 (2010).
- J. van der Oost, M. M. Jore, E. R. Westra, M. Lundgren, S. J. Brouns, *Trends Biochem. Sci.* **38**, 401 (2009).
- R. Jansen, J. D. Embden, W. Gaastra, L. M. Schouls, *Mol. Microbiol.* **43**, 1565 (2002).
- I. Grissa, G. Vergnaud, C. Pourcel, *BMC Bioinformat.* **8**, 172 (2007).
- T. H. Tang *et al.*, *Proc. Natl. Acad. Sci. U.S.A.* **99**, 7536 (2002).
- R. K. Lillestøl, P. Redder, R. A. Garrett, K. Brügger, *Archaea* **2**, 59 (2006).
- R. K. Lillestøl *et al.*, *Mol. Microbiol.* **72**, 259 (2009).
- T. H. Tang *et al.*, *Mol. Microbiol.* **55**, 469 (2005).
- Materials and methods are available as supporting material on *Science Online*.
- A. Ebihara *et al.*, *Protein Sci.* **15**, 1494 (2006).
- L. Holm, C. Sander, *J. Mol. Biol.* **233**, 123 (1993).
- V. Kunin, R. Sorek, P. Hugenholtz, *Genome Biol.* **8**, R61 (2007).
- P. Legault, J. Li, J. Mogridge, L. E. Kay, J. Greenblatt, *Cell* **93**, 289 (1998).
- A. Huppler, L. J. Nikstad, A. M. Allmann, D. A. Brow, S. E. Butcher, *Nat. Struct. Biol.* **9**, 431 (2002).
- Z. Cai *et al.*, *Nat. Struct. Biol.* **5**, 203 (1998).
- X. Ye, A. Gorin, A. D. Ellington, D. J. Patel, *Nat. Struct. Biol.* **3**, 1026 (1996).
- K. Anand, A. Schulte, K. Vogel-Bachmayr, K. Scheffzek, M. Geyer, *Nat. Struct. Mol. Biol.* **15**, 1287 (2008).
- We thank W. Westphal for help with purification of Csy4 constructs; J. van der Oost for discussion; J. Doudna Cate and members of the Doudna laboratory for critical reading of the manuscript; and C. Ralston and J. Holton (Beamlines 8.2.2 and 8.3.1, Advanced Light Source, Lawrence Berkeley National Laboratory) and S. Coyle for assistance with X-ray data collection. R.E.H. is supported by the U.S. NIH training grant 5 T32 GM08295. M.J. is supported by a Human Frontier Science Program Long-Term Fellowship. B.W. is a Howard Hughes Medical Institute Fellow of the Life Sciences Research Foundation. This work was supported in part by grants from NSF and the Bill and Melinda Gates Foundation. J.A.D. is a Howard Hughes Medical Institute Investigator. Coordinates and structure factors for the Csy4-crRNA complex have been deposited in the Protein Data Bank under accession codes 2xli, 2xlj, and 2xlk. The authors have filed a related patent.

Supporting Online Material

www.sciencemag.org/cgi/content/full/329/5997/1355/DC1
Materials and Methods
Figs. S1 to S10
Table S1
References

13 May 2010; accepted 22 July 2010
10.1126/science.1192272

Prediction of Individual Brain Maturity Using fMRI

Nico U. F. Dosenbach,^{1*} Binyam Nardos,¹ Alexander L. Cohen,¹ Damien A. Fair,² Jonathan D. Power,¹ Jessica A. Church,¹ Steven M. Nelson,^{1,3} Gagan S. Wig,^{1,4,5} Alecia C. Vogel,¹ Christina N. Lessov-Schlaggar,⁶ Kelly Anne Barnes,¹ Joseph W. Dubis,¹ Eric Feczkó,⁶ Rebecca S. Coalson,^{1,7} John R. Pruett Jr.,⁶ Deanna M. Barch,^{3,6,7} Steven E. Petersen,^{1,3,7,8} Bradley L. Schlaggar,^{1,7,8,9*}

Group functional connectivity magnetic resonance imaging (fcMRI) studies have documented reliable changes in human functional brain maturity over development. Here we show that support vector machine-based multivariate pattern analysis extracts sufficient information from fcMRI data to make accurate predictions about individuals' brain maturity across development. The use of only 5 minutes of resting-state fcMRI data from 238 scans of typically developing volunteers (ages 7 to 30 years) allowed prediction of individual brain maturity as a functional connectivity maturation index. The resultant functional maturation curve accounted for 55% of the sample variance and followed a nonlinear asymptotic growth curve shape. The greatest relative contribution to predicting individual brain maturity was made by the weakening of short-range functional connections between the adult brain's major functional networks.

Functional magnetic resonance imaging (fMRI) holds the promise that it may one day aid in the diagnosis of developmental delays and neuropsychiatric disorders, especially for conditions that lack structural brain abnormalities. Much progress has been made describing typical and atypical human brain activity at the group level with use of fMRI. However,

determining whether single fMRI scans contain sufficient information to classify and make predictions about individuals remains a critical challenge (1).

The work described here had two major objectives. The first aim was to develop an approach for making accurate predictions about individuals on the basis of single fMRI scans. The

second aim, building on the first, was to further illuminate typical brain development, a prerequisite for studying developmental disorders and pediatric-onset neuropsychiatric diseases (2, 3).

Previous developmental fMRI studies have shown reliable differences between children and adults (4–9). Thus, we set out to push the study of functional brain maturation toward making predictions about single individuals. We used multivariate pattern analysis (MVPA) tools (10–14) to make continuously valued predictions about the relative functional maturity levels of individual brains.

¹Department of Neurology, Washington University School of Medicine, St. Louis, MO 63110, USA. ²Department of Psychiatry, Oregon Health and Science University, Portland, OR 97239, USA. ³Department of Psychology, Washington University, St. Louis, MO 63130, USA. ⁴Department of Psychology, Harvard University, Cambridge, MA 02138, USA. ⁵Athinoula A. Martinos Center for Biomedical Imaging, Massachusetts General Hospital, Charlestown, MA 02129, USA. ⁶Department of Psychiatry, Washington University School of Medicine, St. Louis, MO 63110, USA. ⁷Department of Radiology, Washington University School of Medicine, St. Louis, MO 63110, USA. ⁸Department of Anatomy and Neurobiology, Washington University School of Medicine, St. Louis, MO 63110, USA. ⁹Department of Pediatrics, Washington University School of Medicine, St. Louis, MO 63110, USA.

*To whom correspondence should be addressed. E-mail: ndosenbach@wustl.edu (N.U.F.D.); schlaggarb@neuro.wustl.edu (B.L.S.)

MVPA applies sophisticated machine-learning algorithms (12, 14) to the complex patterns generated by a myriad of measurements, termed features. We chose support vector machines (SVMs) as our classification and prediction algorithms because they are resilient to overfitting and allow the extraction of feature weights (15, 16). Because of its sensitivity, MVPA has become increasingly used in task-evoked neuroimaging, beginning with early work by Haxby and colleagues (10). When applied to task-related fMRI data, MVPA has allowed researchers to accomplish impressive feats, such as extracting patterns related to memory reinstatement (17), predicting which nouns participants heard (18), and exploring the neural correlates of consciousness (19, 20).

However, in many pediatric and clinical populations, the acquisition of task-related data becomes increasingly difficult because of a variety of causes (e.g., ability to perform task). Therefore, we used functional connectivity MRI (fcMRI) data, which can be collected quickly and easily under different conditions, including but not limited to anesthesia, sleep, and quiet rest (21). Resting-state fcMRI (rs-fcMRI) studies measure the correlations in spontaneous activity between brain regions (22). These rs-fcMRI measurements are reliable across scans and institutions (23) and are thought to have been shaped by the cumulative effect of experiences across one's lifespan (24).

Thus, we developed a functional connectivity MVPA (fcMVPA) approach that combines the sensitivity of MVPA with the robust and easy data acquisition of fcMRI. To build a machine that could predict the functional maturity level of individual brains from about 5 min of fMRI data, we used 238 rs-fcMRI scans (3 T; continuous rest) from typically developing participants ranging in age from 7 to 30 years (tables S1 and S2). Blood oxygen level-dependent (BOLD) time courses

were generated for 160 regions of interest (ROIs) derived from a series of meta-analyses of task-related fMRI studies that cover much of the brain (fig. S1 and table S3). All possible interregional temporal correlations, or functional connections ($n = 12,720$), were computed for each individual. By using standard MVPA methodology to avoid circularity bias (14), we first reduced the number of features to the 200 functional connections most reliably different between children and adults in each round of leave-one-out cross-validation (16).

Binary SVM classification of individuals as either children (61 scans of 7- to 11-year-olds; mean = 9.4) or adults (61 scans of 24- to 30-year-olds; mean = 26.2), matched for brain volume and in-scanner movement, was 91% accurate (permutation test, $P < 0.0001$; 90% sensitive; 92% specific).

To assess the relative functional brain maturity of individuals more precisely, we used SVM regression (SVR). Chronological age served as the training measure for SVR brain maturity prediction because, in contrast to other potential measures of maturity such as hormone levels or developmental milestones, age is easily obtained and free of measurement error. In this manner, we generated a predicted "brain age" as an estimate of each participants' functional maturity level. Achieving functional brain maturity in this sense is likely the consequence of integrated processes that are both developmental (e.g., myelination and synaptic pruning) and experiential.

The predicted brain ages for all scans were converted to a functional connectivity maturation index (fcMI) by setting the mean predicted brain age of typically developed young adults (18 to 30 years old) equal to 1.0. The fcMI thus represents a 200-dimensional, weighted index of an individual's overall functional brain maturity.

Model selection analyses were carried out by using Akaike information criterion (AIC) weights

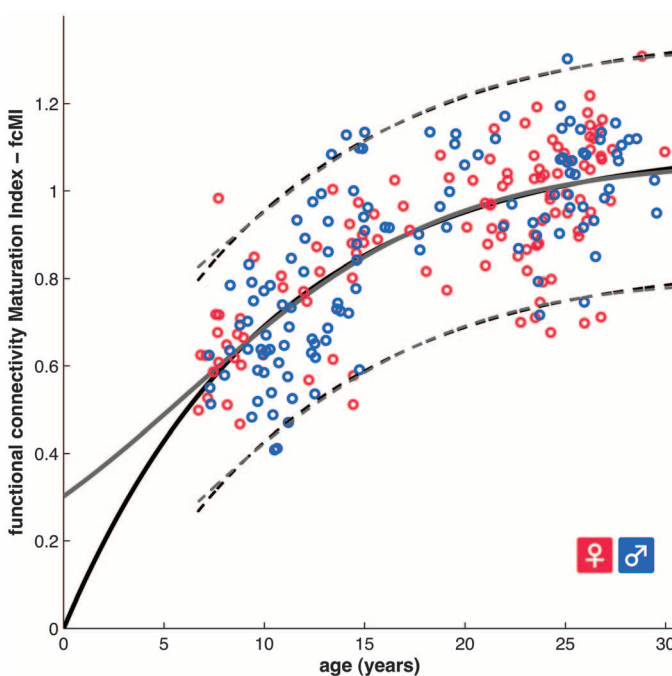
(16, 25). These analyses showed that functional maturity levels between the ages of 7 and 30 years, as measured by fcMI, are best fit by classic biological models of asymptotic growth or maturation (26), such as Von Bertalanffy's growth curve or the Pearl-Reed logistic growth curve (Fig. 1 and table S4).

The most probable models of functional brain maturation provided almost identical curve fits in the 7- to 30-years-old age range (Fig. 1 and fig. S2). Linear models generated the poorest fits (fig. S2 and table S4). The best fitting models showed asymptotic maturation toward a predicted population mean maximum brain age of ~22 years, corresponding to an fcMI of slightly greater than 1.0. The fitted models mainly differed in their predictions for younger ages. The two-parameter Von Bertalanffy curve predicts more rapid maturation between birth and age 7 years than the three-parameter Pearl-Reed curve. Future collection of additional rs-fcMRI scans between birth and age 7 years should help decide between these interesting alternatives.

For independent replication, the same analyses were also carried out on two other large-scale developmental functional connectivity data sets with somewhat different characteristics. Data set 2 consisted of 195 fcMRI scans (age 7 to 31 years; 1.5 T) where rest periods had been extracted from blocked fMRI designs. Data set 3 consisted of 186 event-related fMRI scans (age 6 to 35 years) that were made more similar to resting state by regressing out task effects. Despite these differences in the type of functional connectivity data, binary adult-versus-child classification results replicated (accuracy of 92% for data set 2 and 93% data set 3), as did the functional brain maturity prediction results (data set 2, $r^2 = 0.519$; data set 3, $r^2 = 0.557$) (figs. S3 and S4, and table S4). After separately generating fcMI values for each data set, 613 scans between the ages of 6 and 30 years were combined into a single, "mixed-type" functional connectivity maturation curve (figs. S5 and S6), with very similar properties to the pure 3-T rs-fcMRI maturation curve (Fig. 1). Six participants older than 30 years from data sets 2 and 3 were excluded from the fits for consistency across data sets. These findings demonstrate that fcMRI-based maturation analyses generalize across cohorts and different types of fcMRI data.

A crucial aspect of MVPA is displaying and analyzing the features that drive the multivariate predictor. Therefore, we extracted the weighting assigned to each feature (i.e., functional connection) by the predictor and displayed the 156 consensus features (16) from the SVR maturity prediction (data set 1) scaled by their weights (Fig. 2 and fig. S7). The resulting pattern of feature weights verified and expanded on findings from prior developmental rs-fcMRI studies (7, 8, 27). These previous studies, which were based on smaller sets of regions and sample numbers, had suggested that the brain's functional organization is dominated by more local

Fig. 1. Functional brain maturation curve. Individual functional brain maturity levels of 238 rs-fcMRI scans (115 females) between the ages of 7 to 30 years. Chronological age is shown on the x axis and the fcMI on the y axis (females pink, males blue). The fit for the Von Bertalanffy's equation [$a \cdot (1 - e^{-bx})$, $r^2 = 0.553$, permutation test, $P < 0.001$, AIC weight = 0.3] is shown with a solid black line. The fit for the Pearl-Reed equation [$a/(1 + b \cdot e^{-cx})$, $r^2 = 0.555$, AIC weight = 0.23] is shown with a solid gray line. The 95% prediction limits are shown with dashed lines.



interactions between brain regions in children and shifts to a more distributed architecture in young adults.

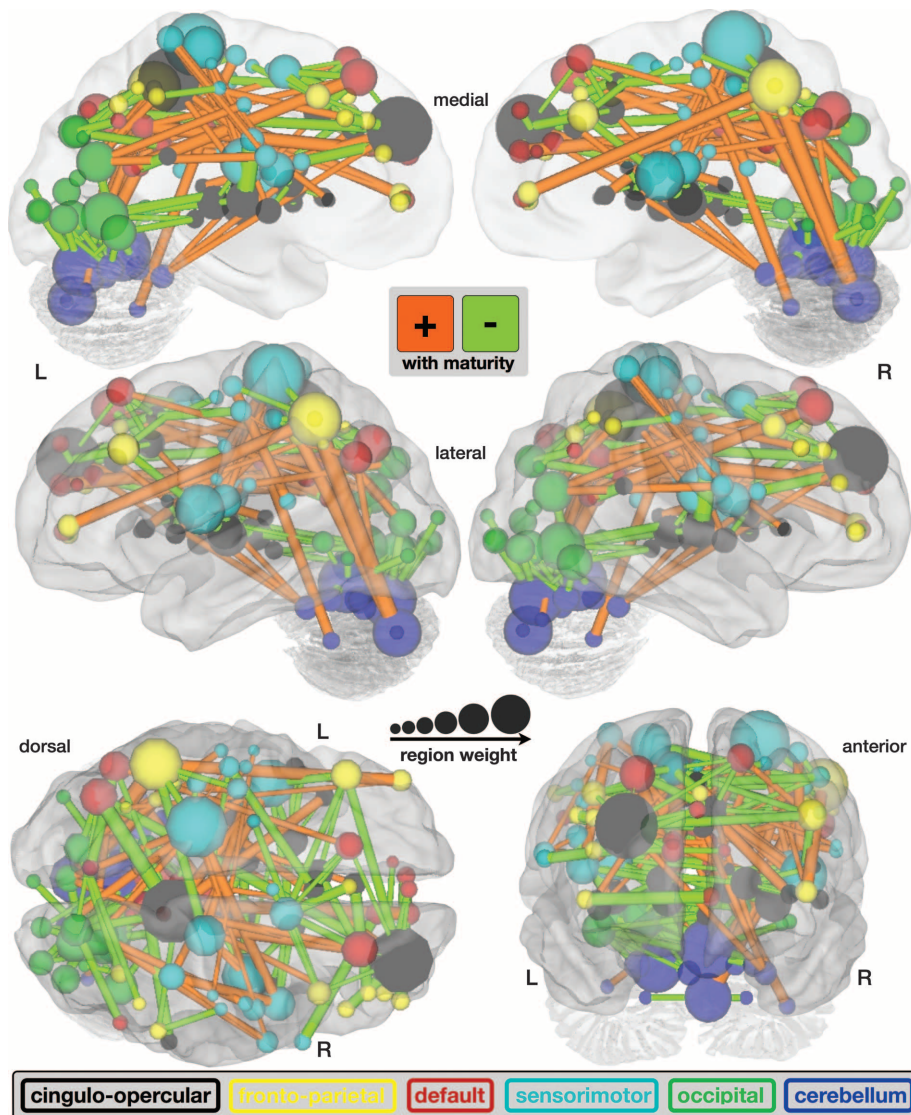


Fig. 2. fcMVPA connection and region weights. The functional connections driving the SVR brain maturity predictor are displayed on a surface rendering of the brain. The thicknesses of the 156 consensus functional connections scale with their weights. Connections positively correlated with age are shown in orange, whereas connections negatively correlated with age are shown in light green. Also displayed are the 160 ROIs scaled by their weights (1/2 sum of the weights of all the connections to and from that ROI). The ROIs are color-coded according to the adult rs-fcMRI networks (cingulo-opercular, black; frontoparietal, yellow; default, red; sensorimotor, cyan; occipital, green; and cerebellum, dark blue).

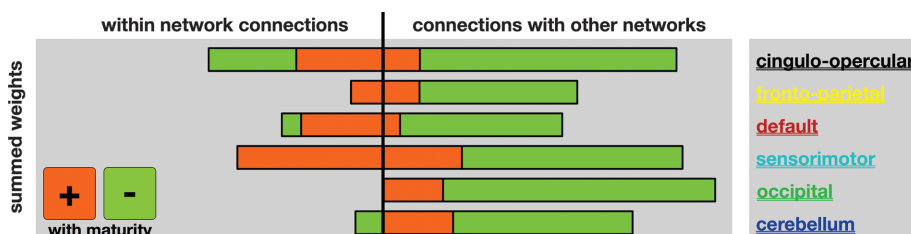


Fig. 3. SVR brain maturity weights by adult rs-fcMRI networks. The sums of all the functional connection weights within each network are shown to the left of the vertical black line. The sums of all the functional connection weights between networks are shown to the right.

The fcMVPA brain maturity predictor has its basis in two types of functional connections, those whose strengths were positively correlated

(strengthening) with chronological age and those that were negatively correlated (weakening) with chronological age (Fig. 2, figs. S7 and S8, and table S5). As previously noted (7, 8, 27), functional connections that grew in strength across development were significantly longer (mean = 80 mm) than functional connections that diminished in strength (37 mm) [$t(154) = 14.66, P < 1 \times 10^{-30}$] (figs. S7 and S8). In addition, we found that functional connections increasing in strength were significantly more likely to run along the anterior-posterior (AP) axis in the horizontal plane (mean angle = 37°) than the functional connections that became weaker (58°) [$t(154) = 4.84, P < 1 \times 10^{-5}$]. The quantitative nature of the MVPA approach also allowed us to extract the relative contributions of weakening and strengthening functional connections. These analyses revealed that weakening connections contributed more to predicting brain maturity (68%) than strengthening connections (32%), a finding better visualized by separately summing weights for both weakening and strengthening features (Fig. 3).

To extract the relative contributions of different ROIs to maturity prediction, we computed their node or ROI weights by summing the weights across all functional connections for each ROI (Fig. 2, fig. S9, and table S6).

Some of the regions in ventromedial prefrontal cortex and parietal cortex have previously been associated with the brain's default-mode network (28), whereas other anterior, dorsolateral, and medial prefrontal regions are known to be important for cognitive control (4, 6, 29). Hence, we assessed the network affiliations of each ROI more formally by performing modularity optimization on the average adult functional connectivity matrix (8). Doing so partitioned the 160 ROIs into six networks: cingulo-opercular, frontoparietal, default mode, sensorimotor, occipital, and cerebellar (Figs. 2 and 3 and fig. S9) (8, 30).

Separately summing the feature weights for each network (Fig. 3) revealed that the cingulo-opercular control network had the greatest sum total of feature weights, meaning that it was the relatively best predictor, but all six identified networks made sizeable contributions toward predicting functional maturity. Separating functional connection weights according to whether the connections occur within or between networks (Fig. 3) revealed that the vast majority of predictor weights for within-network connections were assigned to strengthening connections (Fig. 3, left). In contrast, most of the weights for between-network connections were taken up by connections that weaken (Fig. 3, right). This pattern is consistent with the internal strengthening of the adult brains' six identified major functional networks, as well as the sharpening of the boundaries between them.

The region with the greatest relative prediction power about brain maturity was the right anterior prefrontal cortex [Montreal Neurological Institute (MNI): 27, 49, 26], thought to be important for cognitive control and higher-order

reasoning (4, 6, 9, 29). The precuneus, which has recently been found to be the most highly structurally (31) and functionally (32) connected brain region, contained the second most predictive ROI (MNI: 8, -40, 50). It stands to reason that regions such as those in the precuneus, situated at the center of the adult brain's connectome, could carry much information about how the network develops.

The results presented here strongly suggest that the fcMVPA approach derives its accuracy from important neurophysiologic changes. The functional connectivity maturation curve (Fig. 1 and fig. S6) has a biologically plausible asymptotic shape, first used to describe the growth of animals (Von Bertalanffy) and human populations in the setting of limited resources (Pearl-Reed) (26). Similarly shaped growth curves that plot measures such as height and head circumference against age are used routinely in pediatric medicine. The maturation curves suggest that mean population functional brain maturity asymptotes toward a maturity level or brain age of ~22 years (33). The shape of the functional maturation curve highlights the nonlinear nature of functional brain maturation (34, 35).

The pattern of fcMVPA feature weights indicated that functional maturation is driven both by the segregation of nearby functional areas, through the weakening of short-range functional connections, and the integration of distant regions into functional networks, by strengthening of long-range functional connections (fig. S7) (2, 7, 8, 27). It is interesting that fcMVPA revealed the relatively greater importance of functional segregation when compared to functional integration for the prediction of functional brain maturity. In addition, fcMVPA showed that functional integration is mainly carried by longer-range functional connections along the AP axis. Grouping brain regions into functional networks (8) showed that both integration within functional networks and segregation between them are widely distributed across the cortex and cerebellum.

Several important, large-scale structural MRI studies of brain maturation have already mapped out anatomical maturation curves for a variety of measures (33, 34, 36, 37). The present study provides a functional counterpart to the prior anatomical studies. In addition, it combines the most relevant features into a single index instead of separately listing different measures. It should be

informative to apply similar MVPA methods to the study of structural brain maturation, as well as combining MVPA of structural and functional data.

Important group-level rs-fcMRI studies have already shown differences in spontaneous activity in disorders such as autism, schizophrenia, depression, and attention-deficit hyperactivity disorder (21). Hence, imaging-based binary classification studies of clinical populations are starting to be pursued (38). The use of SVR in fcMVPA to make continuously valued predictions may become relevant in clinical scenarios where binary classification is insufficient (e.g., to predict years until Alzheimer's disease symptom onset).

The standard clinical workup for many developmental neuropsychiatric disorders already includes a structural MRI scan of the brain. The present observations suggest that the addition, at little extra cost, of a brief resting acquisition to the standard clinical study could one day provide useful information to aid in the screening, diagnosis, and prognosis of individuals with disordered brain function.

References and Notes

- R. A. Poldrack, Y. O. Halchenko, S. J. Hanson, *Psychol. Sci.* **20**, 1364 (2009).
- M. H. Johnson, *Nat. Rev. Neurosci.* **2**, 475 (2001).
- T. Paus, M. Keshavan, J. N. Giedd, *Nat. Rev. Neurosci.* **9**, 947 (2008).
- S. A. Bunge, N. M. Dudukovic, M. E. Thomason, C. J. Vaidya, J. D. E. Gabrieli, *Neuron* **33**, 301 (2002).
- B. L. Schlaggar et al., *Science* **296**, 1476 (2002).
- E. A. Crone, C. Wendelken, S. Donohue, L. van Leijenhorst, S. A. Bunge, *Proc. Natl. Acad. Sci. U.S.A.* **103**, 9315 (2006).
- D. A. Fair et al., *Proc. Natl. Acad. Sci. U.S.A.* **104**, 13507 (2007).
- D. A. Fair et al., *PLOS Comput. Biol.* **5**, e1000381 (2009).
- K. Velanova, M. E. Wheeler, B. Luna, *J. Neurosci.* **29**, 12558 (2009).
- J. V. Haxby et al., *Science* **293**, 2425 (2001).
- S. M. Polyn, V. S. Natu, J. D. Cohen, K. A. Norman, *Science* **310**, 1963 (2005).
- K. A. Norman, S. M. Polyn, G. J. Detre, J. V. Haxby, *Trends Cogn. Sci.* **10**, 424 (2006).
- E. Formisano, F. De Martino, M. Bonte, R. Goebel, *Science* **322**, 970 (2008).
- F. Pereira, T. M. Mitchell, M. Botvinick, *Neuroimage* **45**, S199 (2009).
- A. Ben-Hur et al., *PLOS Comput. Biol.* **4**, e1000173 (2008).
- Materials and methods are available as supporting material on *Science* Online.
- J. D. Johnson, S. G. R. McDuff, M. D. Rugg, K. A. Norman, *Neuron* **63**, 697 (2009).
- T. M. Mitchell et al., *Science* **320**, 1191 (2008).
- C. S. Soon, M. Brass, H.-J. Heinze, J.-D. Haynes, *Nat. Neurosci.* **11**, 543 (2008).
- A. Schurger, F. Pereira, A. Treisman, J. D. Cohen, *Science* **327**, 97 (2010); published online 12 November 2009 (10.1126/science.1180029).
- D. Zhang, M. E. Raichle, *Nat. Rev. Neurol.* **6**, 15 (2010).
- B. B. Biswal, F. Z. Yetkin, V. M. Haughton, J. S. Hyde, *Magn. Reson. Med.* **34**, 537 (1995).
- B. B. Biswal et al., *Proc. Natl. Acad. Sci. U.S.A.* **107**, 4734 (2010).
- C. M. Lewis, A. Baldassarre, G. Committeri, G. L. Romani, M. Corbetta, *Proc. Natl. Acad. Sci. U.S.A.* **106**, 17558 (2009).
- H. Akaike, in *Second International Symposium on Inference Theory*, B. N. Petrov, F. Csaki, Eds. (Akademiai Kiado, Budapest, 1973), pp. 267–281.
- A. Tsouilaris, J. Wallace, *Math. Biosci.* **179**, 21 (2002).
- K. Supekar, M. Musen, V. Menon, K. J. Friston, *PLoS Biol.* **7**, e1000157 (2009).
- M. E. Raichle et al., *Proc. Natl. Acad. Sci. U.S.A.* **98**, 676 (2001).
- N. U. F. Dosenbach et al., *Neuron* **50**, 799 (2006).
- N. U. F. Dosenbach et al., *Proc. Natl. Acad. Sci. U.S.A.* **104**, 11073 (2007).
- P. Hagmann et al., *PLoS Biol.* **6**, e159 (2008).
- D. Tomasi, N. D. Volkow, *Proc. Natl. Acad. Sci. U.S.A.* **107**, 9885 (2010).
- F. I. M. Craik, E. Bialystok, *Trends Cogn. Sci.* **10**, 131 (2006).
- P. Shaw et al., *J. Neurosci.* **28**, 3586 (2008).
- L. H. Somerville, B. J. Casey, *Curr. Opin. Neurobiol.* **20**, 236 (2010).
- P. Shaw et al., *Nature* **440**, 676 (2006).
- G. Gong et al., *J. Neurosci.* **29**, 15684 (2009).
- H. Shen, L. Wang, Y. Liu, D. Hu, *Neuroimage* **49**, 3110 (2010).
- This work was supported by NIH grants NS55582, NS053425, HD057076, and NS00169011 (B.L.S.); NS51281, NS32979, NS41255, and NS46424 (S.E.P.); DA027046 (C.N.L.-S.); EY16336 (J.R.P.); and MH62130 (D.M.B.) and by the John Merck Scholars Fund (B.L.S.), Burroughs-Wellcome Fund (B.L.S.), Dana Foundation (B.L.S.), Ogle Family Fund (B.L.S.), McDonnell Center (S.E.P. and B.L.S.), Simons Foundation (S.E.P.), American Hearing Research Foundation (J. E. C. Lieu), and Diabetes Research Center at Washington University (T. G. Hershey). We thank J. E. C. Lieu, C. E. Pizoli, and T. G. Hershey for providing data and F. M. Miezin, J. Harwell, A. Z. Snyder, and H. M. Lugar for help with data analysis.

Supporting Online Material

www.sciencemag.org/cgi/content/full/329/5997/1358/DC1

Materials and Methods

SOM Text

Figs. S1 to S9

Tables S1 to S6

References

23 June 2010; accepted 4 August 2010
10.1126/science.1194144

ERRATUM

Post date 5 November 2010

Reports: "Prediction of individual brain maturity using fMRI" by N. U. F. Dosenbach *et al.* (10 September, p. 1358). In Fig. 2, the labels in the bottom-right image (anterior view) were incorrect. The "L" and "R" labels should be switched.

Originally published 10 September 2010; corrected: 1 October 2010



www.sciencemag.org/cgi/content/full/329/5997/1358/DC1

Supporting Online Material for

Prediction of Individual Brain Maturity Using fMRI

Nico U. F. Dosenbach,* Binyam Nardos, Alexander L. Cohen, Damien A. Fair, Jonathan D. Power, Jessica A. Church, Steven M. Nelson, Gagan S. Wig, Alecia C. Vogel, Christina N. Lessov-Schlaggar, Kelly Anne Barnes, Joseph W. Dubis,¹ Eric Feczko, Rebecca S. Coalson, John R. Pruett Jr., Deanna M. Barch, Steven E. Petersen, Bradley L. Schlaggar*

*To whom correspondence should be addressed. E-mail: ndosenbach@wustl.edu
(N.U.F.D.); schlaggarb@neuro.wustl.edu (B.L.S.)

Published 10 September 2010, *Science* **329**, 1358 (2010)
DOI: 10.1126/science.1194144

This PDF file includes:

Materials and Methods
SOM Text
Figs. S1 to S9
Tables S1 to S6
References

Correction: Left and right hemisphere labels in bottom-right images of Figs. S1, S7, and S9 and coordinates in Table S5 were corrected.

Supporting Online Material

Materials and Methods

Subjects

Subjects were recruited from Washington University in St. Louis and the surrounding community. Individuals with metal implants, heart arrhythmias, claustrophobia or a history of developmental delay, neurological or psychiatric illness, including the use of psychotropic medications, were excluded. All subjects were native English speakers. All adult subjects gave informed consent, and subjects under the age of 18 years gave assent with parental informed consent, all in accordance with the guidelines and approval of the Washington University Human Studies Committee. Children were acclimated to the MRI environment through the use of a mock scanner prior to data collection. Subjects were reimbursed for their participation.

Data sets

The analyses described in this article utilized three separate developmental functional MRI (fMRI) data sets (Table S1, S2). Unless specifically noted, these data sets were treated identically in processing and analysis.

Data set 1 (Table S2) consisted of a total of 238 resting-state fMRI scans (age 7-30 years; 115 female, 123 male), from 192 individuals, matched across chronological age for total intracranial volume (6.7-17.8 years, mean = 1463 cm³; 18.1-30 years, mean = 1460 cm³; correlation, r = 0.044, P = 0.50) and movement (6.7-17.8 years, mean rms-variance = 0.28 mm; 18.1-30 years, mean rms-variance = 0.31 mm; correlation, r = -0.014, P = 0.83). Two adults were left-handed. For all scans, data were 126 MR frames of continuous resting-state. These data were used for all primary analyses, including brain maturity classification and prediction (Fig. 1, 2, and 3).

Data set 2 (Table S2) consisted of a total of 195 resting-state fMRI scans (age 7-31 years; 101 female, 94 male), from 183 individuals, matched across chronological age for total intracranial volume (7-15.7 years, mean = 1409 cm³; 19-31.4 years, mean = 1421 cm³; correlation, r = 0.086; P = 0.23) and movement (7-15.7 years mean rms-variance = 0.51 mm; 19-31.4 years mean rms-variance = 0.50 mm; correlation, r = -0.092; P = 0.20). One teenage subject was left-handed. For 174 scans, rest data were taken from rest periods of mixed blocked/event-related fMRI designs (1). For nine scans, data were from rest-only paradigms. From each scan 128 MR frames of relaxed resting-state were utilized.

Data set 3 (Table S2) consisted of 186 event-related fMRI scans (age 6-35 years; 99 female, 87 male) from 143 individuals performing simple and controlled lexical processing tasks (2, 3), again matched across chronological age for total intracranial volume (5.8-17.8 years, mean = 1409 cm³; 18.6-35.3 years, mean = 1417 cm³; correlation, r = 0.026; P = 0.73) and movement (7-15.7 years, mean rms-variance = 0.30 mm; 18.6-35.3 years, mean rms-variance = 0.35 mm; correlation, r = -0.008; P = 0.92). Five of the children included in the data set were left-handed. These data were made to approximate resting state by regressing out task-related variance as well as the linear trend on a voxel-by-voxel basis, retaining only the baseline in the

general linear model (GLM) (4, 5). These analyses were carried out using in-house statistical software based on IDL (IDL; Research Systems Inc., Boulder, CO), before any resting state functional connectivity (rs-fcMRI) pre-processing steps. From each scan, 128 MR frames of task-removed event-related data were utilized.

Data acquisition

Data set 1 was acquired on a Siemens MAGNETOM Tim Trio 3.0T Scanner with a Siemens 12 channel Head Matrix Coil (Erlangen, Germany), between 03/2007 and 05/2010. A T1-weighted sagittal MPRAGE structural image was obtained (TE = 3.08 ms, TR-partition = 2.4 s, TI = 1000 ms, flip angle = 8°, 176 slices with 1x1x1 mm voxels) (6). A T2-weighted turbo spin echo structural image (TE = 84 ms, TR = 6.8 s, 32 slices with 2x1x4 mm voxels) in the same anatomical plane as the BOLD images was also obtained to improve alignment to an atlas.

Functional images for data set 1 were obtained using a BOLD contrast sensitive gradient echo echo-planar sequence (TE = 27 ms, flip angle = 90°, in-plane resolution= 4x4 mm; volume TR = 2.5 s for 197 scans; volume TR = 2.2 s for 27 scans; volume TR = 2 s for 14 scans).

Whole brain coverage for the functional data was obtained using 32 contiguous interleaved 4 mm axial slices.

Data sets 2 and 3 were acquired on the same Siemens 1.5 Tesla MAGNETOM Vision MRI scanner (Erlangen, Germany), between 05/2000 and 06/2006 in intermingled fashion. All structural images were obtained using a sagittal magnetization-prepared rapid gradient echo (MP-RAGE) three-dimensional T1-weighted sequence (TE = 4 ms, TR = 9.7 ms, TI = 300 ms, flip angle = 12°, 128 slices with 1.25×1×1 mm voxels). Functional images for data set 2 were obtained using an asymmetric spin echo echo-planar sequence sensitive to blood oxygen level-dependent (BOLD) contrast (T2* evolution time = 50 ms, flip angle = 90°, in-plane resolution 3.75×3.75 mm; volume TR = 2.5 s for 186 scans; volume TR = 2.68 s for 9 scans). Magnetization steady state was assumed after 10 seconds.

Functional images for data set 3 were obtained using an asymmetric spin echo echo-planar sequence sensitive to blood oxygen level-dependent (BOLD) contrast (volume TR = 3.08 s, T2* evolution time = 50 ms, flip angle = 90°, in-plane resolution 3.75×3.75 mm). Steady state was assumed after ~ 9 seconds.

For data sets 2 and 3, whole brain coverage for the functional data was obtained using 16 contiguous interleaved 8 mm axial slices, acquired parallel to the plane transecting the anterior and posterior commissure (AC-PC plane).

Data pre-processing

For subjects with more than one fMRI scan, the BOLD data from multiple dates were first aligned to each other and then transformed to the atlas, in order to improve spatial registration. All subsequent operations were performed on the atlas-transformed volumetric timeseries.

Functional images were first processed to reduce artifacts (4, 7). These steps included: (i) removal of a central spike caused by MR signal offset, (ii) correction of odd versus even slice intensity differences attributable to interleaved acquisition without gaps, (iii) correction for head movement within and across runs and (iv) within run intensity normalization to a whole brain

mode value of 1000. Atlas transformation of the functional data was computed for each individual via the MP-RAGE scan. Each run was then resampled in atlas space (8) on an isotropic 3 mm grid combining movement correction and atlas transformation in a single interpolation (9, 10).

Resting state functional connectivity MRI (rs-fcMRI) pre-processing

For rs-fcMRI analyses, several additional preprocessing steps, as previously described (1, 11-15), were utilized to reduce spurious variance unlikely to reflect neuronal activity. These steps included: (1) a temporal band-pass filter ($0.009 \text{ Hz} < f < 0.08 \text{ Hz}$) and spatial smoothing (6 mm full width at half maximum), (2) regression of six parameters obtained by rigid body head motion correction, (3) regression of the whole brain signal averaged across the whole brain, (4) regression of ventricular signal averaged from ventricular regions of interest (ROIs), and (5) regression of white matter signal averaged from white matter ROIs. Regression of first order derivative terms for the whole brain, ventricular, and white matter signals were also included in the correlation pre-processing.

Regions of interest (ROI)

One could argue that the ideal region of interest (ROI) definition approach would be one that respects the organization of the brain into separable functional areas. The more closely the nodes entered into network analyses represent the underlying functional areas of the brain, the more reliable and accurate the descriptions will be (16). Prior network studies have used both functionally (13, 14) and anatomically defined ROIs (17, 18), both of which are valid and important approaches.

In order to gain at least an estimation of the underlying functional area architecture, we chose to functionally define regions of interest from several meta-analyses of fMRI activation studies. Our main goal was to generate a large set of ROIs that broadly cover much of the cerebral cortex and cerebellum (Fig. S1). The cerebellum is difficult to parcellate anatomically, and usually not included in anatomical parcellation schemes. Furthermore, functionally defining ROIs provided additional leverage for interpreting developmental changes since it allowed us to include ROIs whose function we were already familiar with from previous studies.

Building on prior meta-analytic studies (19), a series of five meta-analyses, focused on error-processing, default-mode (task-induced deactivations), memory, language and sensorimotor functions were carried out (Table S3). All fMRI activation data for these meta-analyses were collected on the same Siemens 1.5 Tesla Vision scanner as data set 2 and data set 3.

For the sensorimotor and language meta-analyses, main effect of activation (ANOVA: time as single factor over 7 levels) statistical images, were generated from each included study. To identify voxels that were reliably activated across these studies, the activation images were thresholded at a high Z-score ($Z > 7$). The error (2-factor ANOVA: correctness (2-levels) x time (7-levels)) and memory-related (2-factor ANOVA: oldness (2-levels) x time (7-levels)) meta-analyses relied on statistically weaker interaction effects therefore the thresholds were scaled appropriately lower (error: $Z > 4$; memory: $Z > 2$) (19). The default-mode regions were derived from meta-analyses of both trial-related ($Z > 7$; main effect of deactivation) and sustained deactivations ($Z > 2$). As for the analysis of interactions a lower threshold was applied to the

sustained signals since they are statistically less reliable. Several thresholds were tested initially, and the peaks identified were very similar. Additionally, there was substantial overlap in identified peaks between meta-analyses, and so small differences in peaks identified from a single meta-analysis were offset by redundancies with other meta-analyses.

Voxels passing the threshold were set equal to one and all others equal to zero, creating a mask of significantly activated voxels for each study. The masks for all studies were summed to create a conjunction image, where each voxel carried a value between zero and the number of studies in the meta-analysis, indicating how often voxels were significantly activated across the meta-analysis. After applying a 4 mm smoothing kernel to these images, peak-finding algorithms were used to identify centroids of reliably activated groups of voxels.

Ten mm diameter spheres were centered at the activity peaks for each meta-analysis. ROIs from the separate meta-analyses were then combined by giving priority to ROIs identified by task-induced deactivations (default-mode) and error > correct (control). For overlapping ROIs across the language, memory and sensorimotor meta-analyses, a spatial average location was first computed. Language, memory and sensorimotor-related ROIs were then added at the final step. Previously published cognitive control regions (13, 20) were included in the set of error-processing related regions.

In this manner, a total of 160 ROIs were generated. The distance between all ROI centers was at least 10 mm, thus not allowing any spatial overlap between ROIs. All three-dimensional coordinates reported in the manuscript are in MNI space.

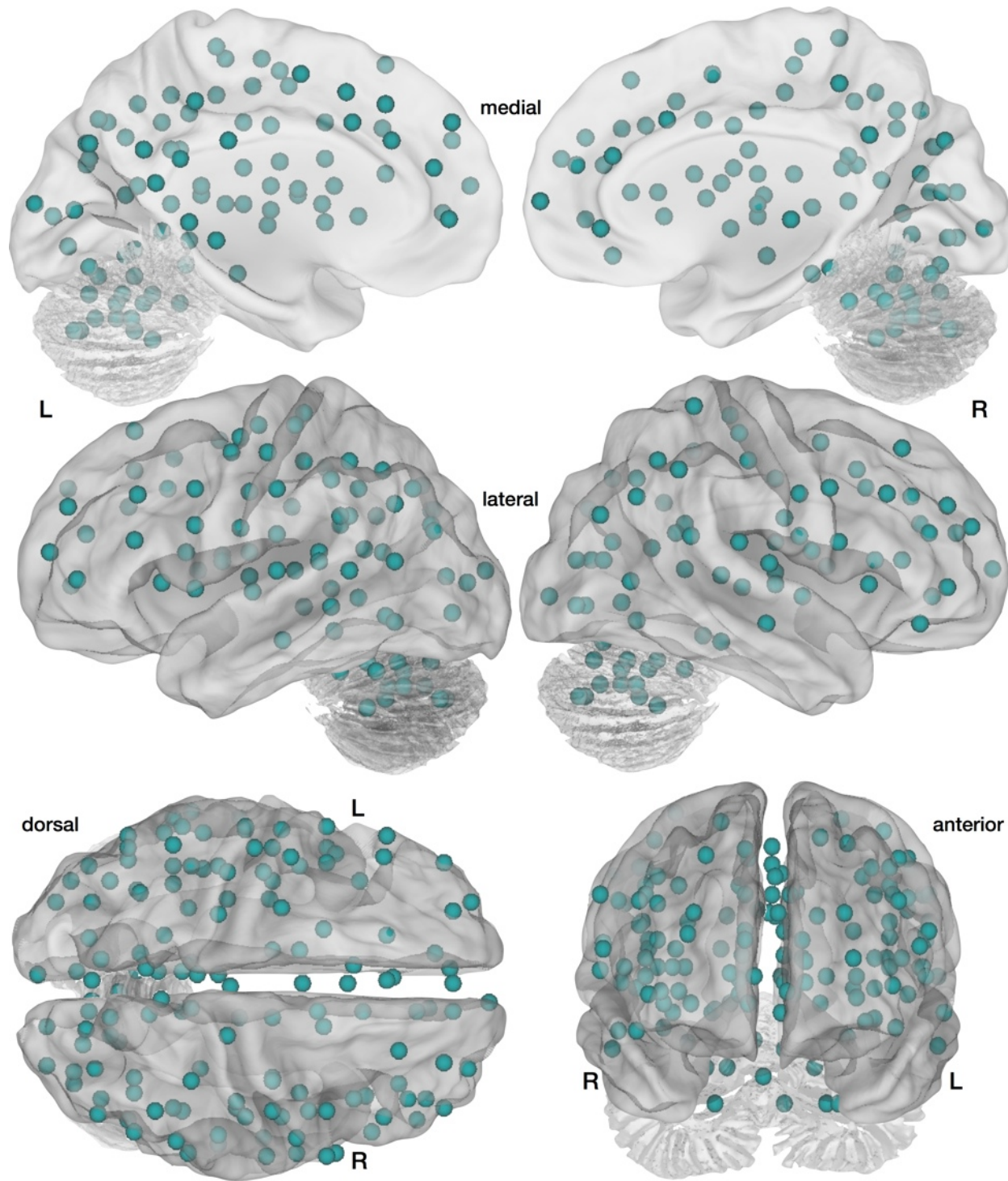


Fig. S1. Regions of interest (ROIs). All 160 ROIs utilized in the analyses are displayed on a surface rendering of the brain (CARET 5.614).

Extraction of functional connections (features)

For every scan, a separate resting state blood oxygenation level dependent (BOLD) timeseries was extracted for each ROI. The BOLD timeseries from each ROI was then correlated

with the BOLD timeseries for every other ROI (Pearson's r), creating a square correlation matrix (160×160) for every scan (13). This resulted in 12,270 correlations between region pairs for each scan. Fisher's z-transform was then applied to the correlation values to ensure normality. These functional connections (Fisher's z-transformed r-values) were the features used in all subsequent multivariate pattern analyses (MVPA).

Support Vector Machine (SVM)

Since first proposed by Vapnik as a logical extension of statistical learning theory, support vector machines (SVMs) have become widely used in the life sciences because of their ability to handle very high-dimensional data, and their accuracy in classification and prediction (21-23). Because of these properties, they have proven powerful in the analysis of structural (24-28) and functional (29, 30) neuroimaging data (31-33).

Accessible and practical discussions of SVM methodology, including visual examples, have been published recently (23, 28, 34). For more detailed theoretical and mathematical explications of SVMs, see (21, 22, 35-39). In light of these explications of SVMs already published, we will only provide a brief overview here.

In SVMs, each of the samples (i.e. subjects) is treated as a point in a multi-dimensional space with as many dimensions as features (i.e. functional connections). In the present study, SVMs were used to discriminate between subjects belonging to two different classes (i.e. child, adult) using soft-margin separation.

In the original hard-margin SVM formulation, the maximally separating hyperplane is found in hyperspace, such that it is as far as possible from the closest members of both classes. This approach finds the largest margin between the decision boundary and the samples nearest to the boundary (support vectors) when correctly classifying all samples.

Often an even larger separating margin can be achieved if some samples are allowed to be misclassified. Hence soft-margin SVM was developed, which finds the maximal margin, while allowing some misclassification. The relative importance of maximizing the margin versus minimizing the amount of misclassification is controlled by the constant C. For a larger C, a larger penalty is assigned to misclassification errors, making the margin smaller or "harder". Theory and experimental results have shown that soft-margin SVMs are less prone to overfitting and will generally provide better performance (23). All SVM classifications described in this article used soft-margin SVMs with the Spider Machine Learning Toolbox (<http://www.kyb.tuebingen.mpg.de/de/bs/people/spider>) default setting of C=1, as suggested (40).

Decision boundaries can be made non-linear using the so-called "kernel trick" (22, 23, 34). This method entails mapping the data points into a higher-dimensional vector space and applying a linear decision function in this higher-dimensional vector space. Even though the decision function is linear in the higher-dimensional vector space, it is non-linear in the original input space. In many cases, nonlinear decision functions provide slightly greater accuracy (23). All SVM classifications and regressions (SVR) described in this article used non-linear decision functions, namely radial basis functions ($k(x,y) = \exp(-|x-y|^2/(2*\sigma^2))$) with $\sigma = 2$, as recommended in the literature (40).

The SVM procedure has two separate phases. During the training phase, the SVM finds the decision boundary. SVM classification is a form of supervised learning since training is done on

labeled samples. Each sample consists of the pattern of features for a given subject and a binary label (either +1 or -1) that identifies the subject as belonging to one of two classes. Once a decision function is learned based on the training data, it can be used to predict the class label of a new, previously unseen, test sample.

In 1997, the SVM approach was extended to include SVM regression (SVR) in order to make real-valued predictions (41). SVR retains some of the main features of SVM classification. A difference between SVM classification and regression is that in classification a loss penalty is incurred for misclassified data (points on the wrong side of the hyperplane), whereas in SVR a penalty is assessed for points too far from the regression line in hyperspace.

Epsilon-insensitive SVR defines a tube of width epsilon around the regression line in hyperspace. Any data points within this tube carry a loss of zero, meaning there is no penalty for being too far away from the regression line. In essence, SVR performs linear regression in hyperspace using epsilon-insensitive loss. In SVR, the C parameter now controls the trade-off between how strongly points beyond the epsilon-insensitive tube are penalized and the flatness of the regression line (larger C allows the regression line to be less flat). All SVR predictions described in this article used epsilon-insensitive SVRs with the Spider Machine Learning Toolbox (<http://www.kyb.tuebingen.mpg.de/de/bs/people/spider>) default setting of C = Infinity, while epsilon was set to 0.00001.

All SVM-related computations were carried out using the Spider Matlab Machine Learning Toolbox (<http://www.kyb.tuebingen.mpg.de/de/bs/people/spider>) implemented in MATLAB 7.8.0 (R2009a; The Mathworks, Natick, MA), as well as functions available as part of the MATLAB Bioinformatics, Curve-fitting and Statistics Toolboxes and in-house MATLAB code.

Cross validation

Leave-one-out-cross-validation (LOOCV) was used to estimate classification (SVM) and prediction (SVR) accuracies (30-32, 42-44). During LOOCV, each sample is designated the test sample in turns while the remaining samples are used to train the SVM classifier or SVR predictor. The decision function derived from the training sample is then used to classify or make a real-valued prediction about the test sample.

In LOOCV, each sample is designated as the test sample once. Hence, there are as many rounds of cross-validation or folds in LOOCV as samples. After all LOOCV folds are completed, the accuracies for all folds are averaged together to generate the final accuracy estimate, which is then reported. The accuracy estimate generated in this way is the expected accuracy of a classifier or predictor on a data set with all but one of the samples (42). LOOCV is a commonly implemented cross-validation tool because it allows using most of the data for training. LOOCV is widely used in machine learning and MVPA approaches (30-32, 42-44) and has been shown to provide a conservative estimate of a classifier's or predictor's true accuracy (42).

Some subjects were scanned more than once, so we performed LOOCV across subjects, not scans (45). For every fold of LOOCV, we left out all the scans of the "left out" single subject. In this manner we avoided so-called "twinning" bias in our accuracy estimates, which can be introduced when a sample very similar to the test sample is included in the training set. Keeping all the scans of an individual together in the same test set eliminated the potential for this type of bias.

All feature ranking and filtering (see immediately below) was always carried out on the training sample only, without examining the labels of the test sample, in order to avoid the introduction of bias.

Feature ranking and elimination

Even though SVMs are designed to contend with high-dimensional feature spaces, studies have shown that initially reducing the number of features can not only speed up computation, but also improve performance (31, 32, 44, 45). Therefore, for both SVM and SVR, an initial univariate feature-filtering step was utilized (31, 32, 44).

For SVM classifications, 12,720 t-tests (two-sided, not assuming equal variance) comparing every feature across the classes were performed separately on the training set of each LOOCV fold. The test samples were excluded prior to t-testing. For each LOOCV fold, the features were then separately ranked by their absolute T-scores in descending order.

For real-valued SVR predictions (i.e. brain maturity), the correlation (Pearson's r) of each of the 12,720 features with the independent variable (i.e. chronological age) was computed on the training set of each LOOCV fold. The test samples were excluded prior to correlating each feature with the independent variable. For each LOOCV fold, the features were then separately ranked by the absolute value of the correlation coefficients with chronological age in descending order.

After univariate feature ranking for both SVM classification and SVR prediction, the highest ranked features were retained while the rest were eliminated. For all analyses reported in this article the feature-filtering cutoff was 200 features. Preliminary analyses on a previously published subset of data set 2 (1) had shown that for SVM classification the 200 highest ranked features, by t-testing, passed Bonferroni's correction at $P = 0.01$. Hence, a cutoff of 200 features was carried forward for all analyses.

Additional preliminary SVM classification analyses (children vs. adults) were also carried out to try to define an optimum number of features. We used recursive feature elimination (RFE) within nested loops of LOOCV (31, 46). In this approach, LOOCV is run again inside the training set of each loop of LOOCV with the aim of identifying an optimum number of features. RFE is a backward feature elimination technique that iteratively removes features (functional connections) from the data set with the aim of removing as many non-informative features as possible while retaining features that carry discriminative information. Although RFE has successfully improved accuracy for other data sets, for the data included in this manuscript, SVM-RFE did not significantly improve accuracy over simply selecting the 200 highest-ranked features. Therefore, SVM-RFE was not used and subsequent analyses relied on simpler feature filtering alone.

Significance testing of classification and prediction accuracies

The statistical significance of all LOOCV results was assessed using permutation testing as proposed by Golland et al. (47). Using this approach we estimated the empirical cumulative distribution of the classifier and predictor accuracies under the null hypothesis (no discriminability). In other words, we estimated how likely we were to have observed the same classification or prediction performance by chance.

For each SVM classification described in this article, the class labels (e.g. child vs. adult) were randomly permuted 10,000 times, and the entire classification process including feature ranking and elimination was carried out with each one of the sets of randomized class labels. The mean accuracies across permutation tests were always 50%, suggesting that the analyses were free of introduced bias.

For the SVR brain maturity predictions described in this article, the prediction labels (i.e. chronological ages) were randomly permuted 1,000 times, and the entire prediction process including feature ranking and elimination was carried out with each one of the sets of randomized prediction labels.

The p-values reported for accuracy represent the probability of observing the reported accuracy by chance ((number of permutation errors < observed error) + 1) / (number of permutations + 1). The reported p-values for the maturity prediction r^2 values represent the probability of observing the reported r^2 values by chance.

Model selection curve fitting and graphing

Model selection for fcMRI maturation curves utilized the Akaike information criterion (AIC), which allows comparison of non-nested models (48-51). The AIC ($2k - 2\ln(L)$; where k = number of parameters and L = maximum likelihood of model) provides a relative goodness of fit estimate for different models when applied to the same data (Table S4). It takes into account both descriptive accuracy and parsimony, since it carries a penalty for increasing the number of free parameters. The absolute AIC values are not particularly meaningful since they are specific to the data set being modeled. The relative AIC values ($\Delta\text{AIC}_i = \text{AIC}_i - \min \text{AIC}$), however, can be used to rank models. The relatively best model is assigned a ΔAIC_i of zero. As a rule of thumb, Akaike suggested that ΔAIC values < 2 indicate that models are almost equivalent. In addition, ΔAIC values can be converted to AIC weights ($w_i\text{AIC}$). To do so, the likelihood of a model is estimated by $L = e^{-1/2\Delta\text{AIC}_i}$. The AIC weight of each model is its likelihood divided by the sum of likelihoods for all models. The AIC weight can be interpreted as the probability that a model is the best model among the set of examined models. Using these methods, seven plausible models with either two or three parameters were analyzed (Table S4).

All curve fitting, graphing and statistical testing was carried out using MATLAB 7.8.0 (R2009a; The Mathworks, Natick, MA) and the MATLAB Statistics and Curve Fitting toolboxes and in-house MATLAB code.

Characterization of functional connections (features)

On every fold of LOOCV, the 200 highest ranked features were selected. Since feature ranking is based on a slightly different subset of the data for each fold of LOOCV, the selected features (i.e. functional connections) differed slightly from fold to fold of LOOCV. However, 156 features were included (i.e. passed feature filtering) on every fold of LOOCV for SVR brain maturity prediction. These “consensus” features were always selected to form part of the predictor (100% overlap). Therefore, all subsequent visualization of feature weights (Fig. 2, Fig. S7, Table S5), feature length and angle (Fig. S3) was restricted to these 156 consensus features. As with prediction accuracy, displayed feature weights (Fig. 2, Fig. S7, Table S5) are the average

across all folds of LOOCV.

Fig. S8 graphs connection length in mm and angle from the anterior-posterior (AP) axis in degrees. The length of functional connections is simply the root-mean-square distance between the centers of the respective ROIs that make up the functional connection, expressed in mm. The displayed connection angles against the AP axis were measured by translating all connections to a common origin. The connections were projected to the horizontal plane and the absolute angle from the AP-axis was measured in degrees.

Characterization of regions of interest (ROI)

The contribution of different ROIs to the prediction of brain maturity was not evenly distributed. Some ROIs formed many strongly weighted consensus functional connections with other ROIs and some did not form any (Fig. 2, Fig. S9, Table S6). To represent the relative contribution of different ROIs to brain maturity prediction we computed the “region weight” for each ROI. To do so we summed the feature weights (i.e. SVR weights for consensus functional connections) for each ROI (Table S6). If an ROI did not form part of any consensus functional connections, it was given a region weight of zero. In Fig. 2 and Fig. S9 the diameters of the spheres representing ROIs are scaled by the ROI’s region strength, in order to visually represent the relative contribution of each ROI to functional brain maturity prediction.

Characterization of adult rs-fcMRI functional connectivity networks

In order to label ROIs according to their rs-fcMRI module membership in young adults, we performed a community detection analysis on our 160 ROI collection (14, 52, 53). We used the ROIs as nodes, and the pairwise correlation coefficient between rs-fcMRI timecourses (mean r of 61 young adult scans ages 25-30 years; movement and brain size matched to children aged 7-11 years) as connections between nodes (14). We used the modularity optimization algorithm of Newman (52). The network partition that was most resistant to perturbation by randomization, as measured by variation of information (VOI) (53, 54) ($r = 0.18$), was used to define the modules or communities seen in Fig. 2 and Fig. S9. A high quality index ($Q = 0.61$) indicated good community structure.

To assess the relative contributions of different rs-fcMRI networks identified in adults to predicted brain maturity, we summed the feature weights across all the ROIs in a given network (Fig. 3). Functional connections were separated based on whether they connected ROIs belonging to the same or different networks (Fig. 3). If a functional connection was between two networks, half of the feature weight was assigned to each network.

Caret visualization

ROIs and functional connections were visualized on a surface rendering of a human brain atlas using CARET 5.614 (55-57). The sizes of the spheres representing ROIs were scaled by their node strengths. The widths of the vectors representing consensus functional connections were scaled by their weights.

Supporting text and figures

Functional connectivity maturation modeling

Seven common growth/maturation models were analyzed using AIC weights (Table S4). For the age range we studied (7-30 years) five of the models (Von Bertalanffy, Pearl-Reed, Von Bertalanffy with y-intercept, log, quadratic) provided almost identical fits (Fig. S2), r^2 values greater than 0.55 and ΔAIC values less than 2 (Table S4). The only two models that fit the data substantially worse were the quadratic constrained to the origin (green in Fig. S2) and the linear (red in Fig. S2). These two models had ΔAIC values greater than 10 and AIC weights close to zero, meaning that the probability of these two models being the relatively best ones was very close to zero.

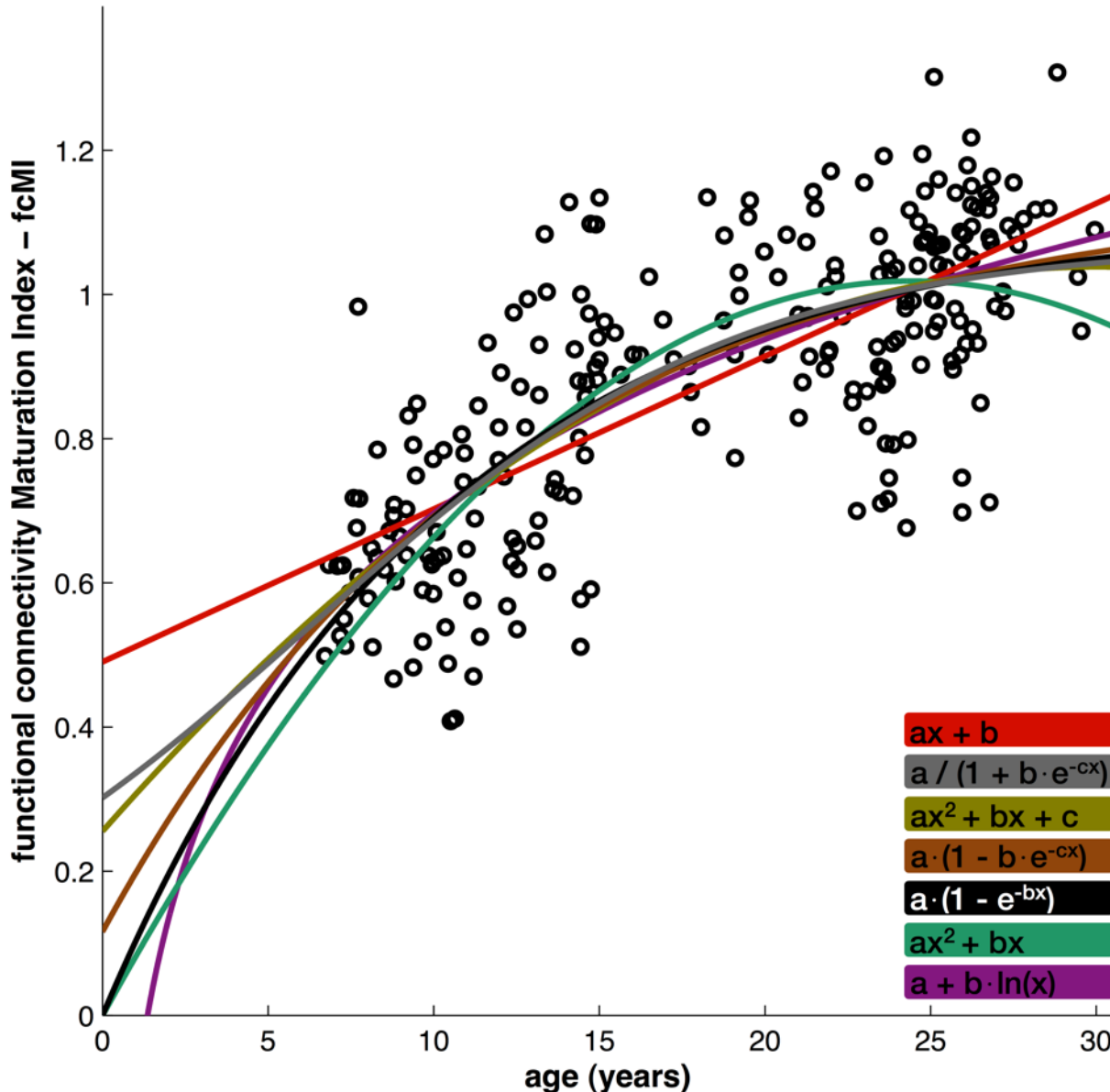


Fig. S2. Individual functional brain maturity levels (black circles) for data set 1. Chronological age is shown on the x-axis and the functional connectivity Maturation Index (fcMI) on the y-axis. Fitted curves for functions included in model selection are shown (linear – red; Pearl-Reed –

gray; quadratic – green/brown; Von Bertalanffy with y-intercept – brown; Von Bertalanffy – black; quadratic constrained to origin – green; log – purple).

The 5 well-fitting maturation models all document asymptotic maturation. The 2- and 3-parameter Von Bertalanffy curves, as well as the Pearl-Reed curve, are classic models of biological growth. Von Bertalanffy developed his equations initially to forecast the growth of sharks, whereas the Pearl-Reed curve provided an early model of human population growth in the face of limited resources (58-61). For these curves, parameter a provides the asymptote that represents the predicted maximum of the population mean. Hence, these models suggest that a “functional brain age” of ~22 years, or an fcMI of slightly greater than 1.0, corresponds to the predicted maximum of the population mean. Since fcMI scores are variable across individuals, some will have fcMI values greater than the mean for their age, or be relatively more mature, and some will have fcMI scores below the mean for their age, suggesting that their functional architecture is relatively less mature.

These models are very similar for the studied age range of 7-30 years old. They mainly differ in their predictions for ages outside of this age-range. For one, they make different predictions for the dynamics of brain maturation between birth and age 7 years. The 2-parameter Von Bertalanffy curve differs from the Pearl-Reed and the 3-parameter Von Bertalanffy curve in that it predicts an fcMI of 0.0 at age 0. Since rs-fcMRI already shows some recognizable organization in infancy (62, 63), this possibility seems less likely than the possibility that newborns already have an fcMI greater than 0.0.

While the shapes of the quadratics are similar to the asymptotic growth curves (Pearl-Reed, Von Bertalanffy) between ages 7-30 years, they make different predictions for ages older than 30 years. In contrast to the classical asymptotic growth curves, the quadratics predict the fcMI to peak and then start declining again with advancing age. While an interesting possibility, this seems biologically less plausible since it would suggest that aging could be constructed as “maturation in reverse” at least to some degree. While continued changes in functional connectivity seem likely after age 30 years, these changes may well be driven by features/functional connections other than the ones used to predict maturation between ages 7-30 years and hence they would not be measured by the fcMI. Future collection of rs-fcMRI scans across the entire lifespan should help distinguish between these interesting alternatives.

Data set 2 replicates classification and prediction accuracy

Data set 2, which consisted of 195 fMRI scans (101 female) matched for head size and movement was different from data set 1 in that for most scans it consisted of 128 MR frames taken from the rest periods of blocked or mixed blocked/event-related fMRI designs (cut & concatenated). Furthermore, data were collected on a 1.5 Tesla scanner, not a 3 Tesla scanner and the distribution of samples across age was also different.

Despite these differences, we were able to replicate our initial child vs. young adult SVM classification accuracy (92%; permutation test, $P < 0.0001$) using 62 scans from children and 62 scans from young adults.

The brain maturity prediction results for data set 2 (Fig. S3, Table S4; two scans older than 30 years excluded from curve fits for consistency) were also very similar to the results from our

main data set. As for the continuous rest data (data set 1), linear provided the relatively worst fit (AIC weight ~ 0). All other models had relatively good fits with r^2 values of 0.51 and better. In contrast, to the continuous rest data (data set 1) both the quadratics provided accurate fits (Table S4). However, the good fits of the quadratics for this data set were mainly driven by a small number of adults older than 25 years with very low fcMI values. Since subjects with ages greater than 25 years were undersampled in data set 2, and the goodness of the quadratic fits was not borne out in the other data sets, we consider these few subjects as outliers towards the relatively functionally immature end of the fcMI spectrum.

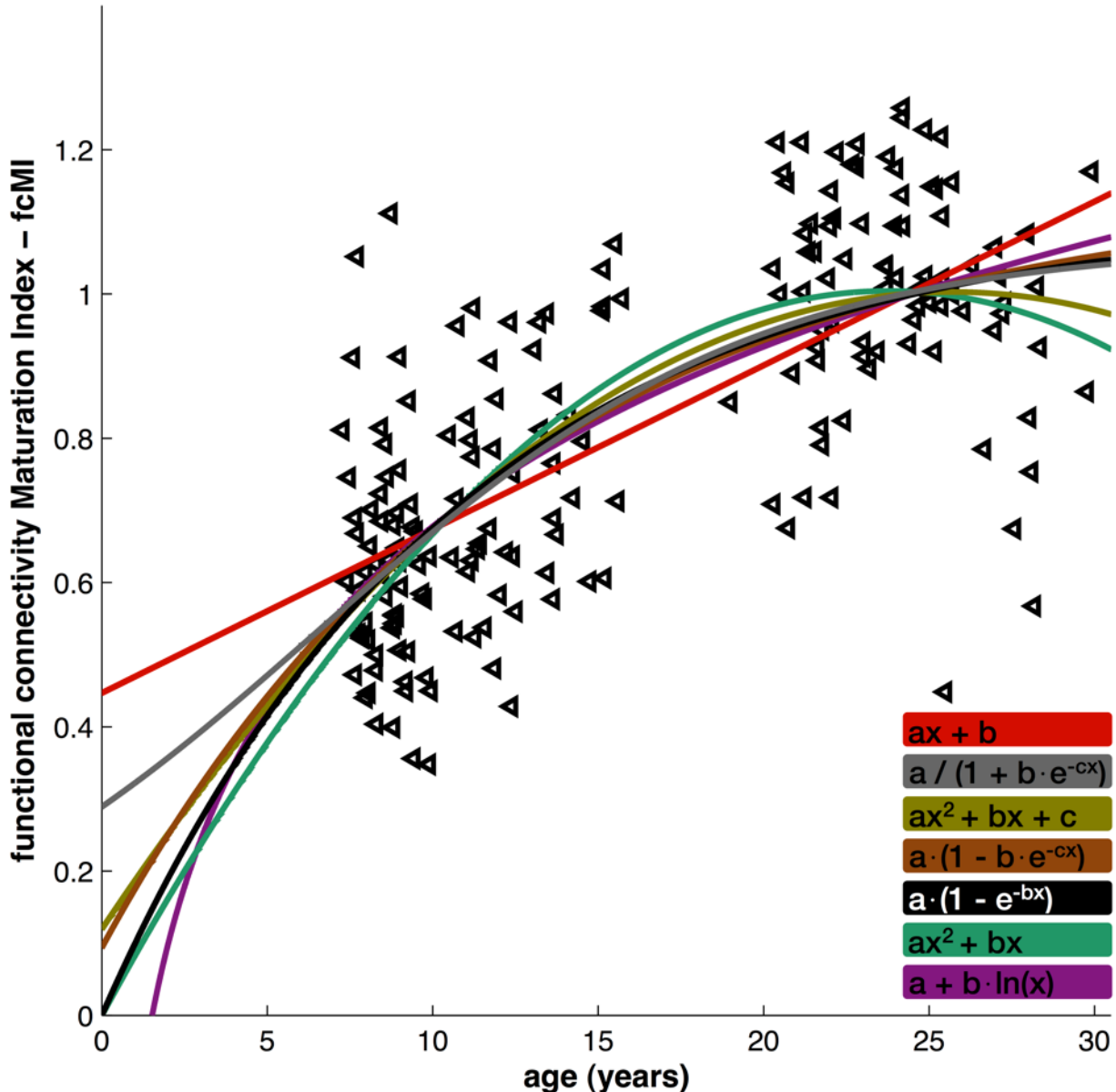


Fig. S3. Individual functional brain maturity levels (black triangles) for data set 2. Chronological age is shown on the x-axis and the functional connectivity Maturation Index (fcMI) on the y-axis. Fitted curves for functions included in model selection are shown (linear – red; Pearl-Reed – gray; quadratic – green/brown; Von Bertalanffy with y-intercept – brown; Von

Bertalanffy – black; quadratic constrained to origin – green; log – purple).

Data set 3 replicates classification and prediction accuracy

Data set 3, which consisted of 186 fMRI scans matched for head size and movement (99 female), was fairly different from both data sets 1 and 2 in that it consisted of 128 MR frames taken from an event-related fMRI design after the task-effects had been regressed out. In addition, the TR was slightly longer (3.08 seconds). The data were collected on a 1.5 Tesla scanner and the distribution of scans across age was different from both data set 1 and data set 2.

Despite these differences, we were able to replicate our initial child vs. young adult SVM classification accuracy (93%; permutation test, $P < 0.0001$) using only 49 scans from children and 49 scans from young adults. The brain maturity prediction results for data set 3 (Fig. S4) were also very similar to the results from data sets 1 and 2.

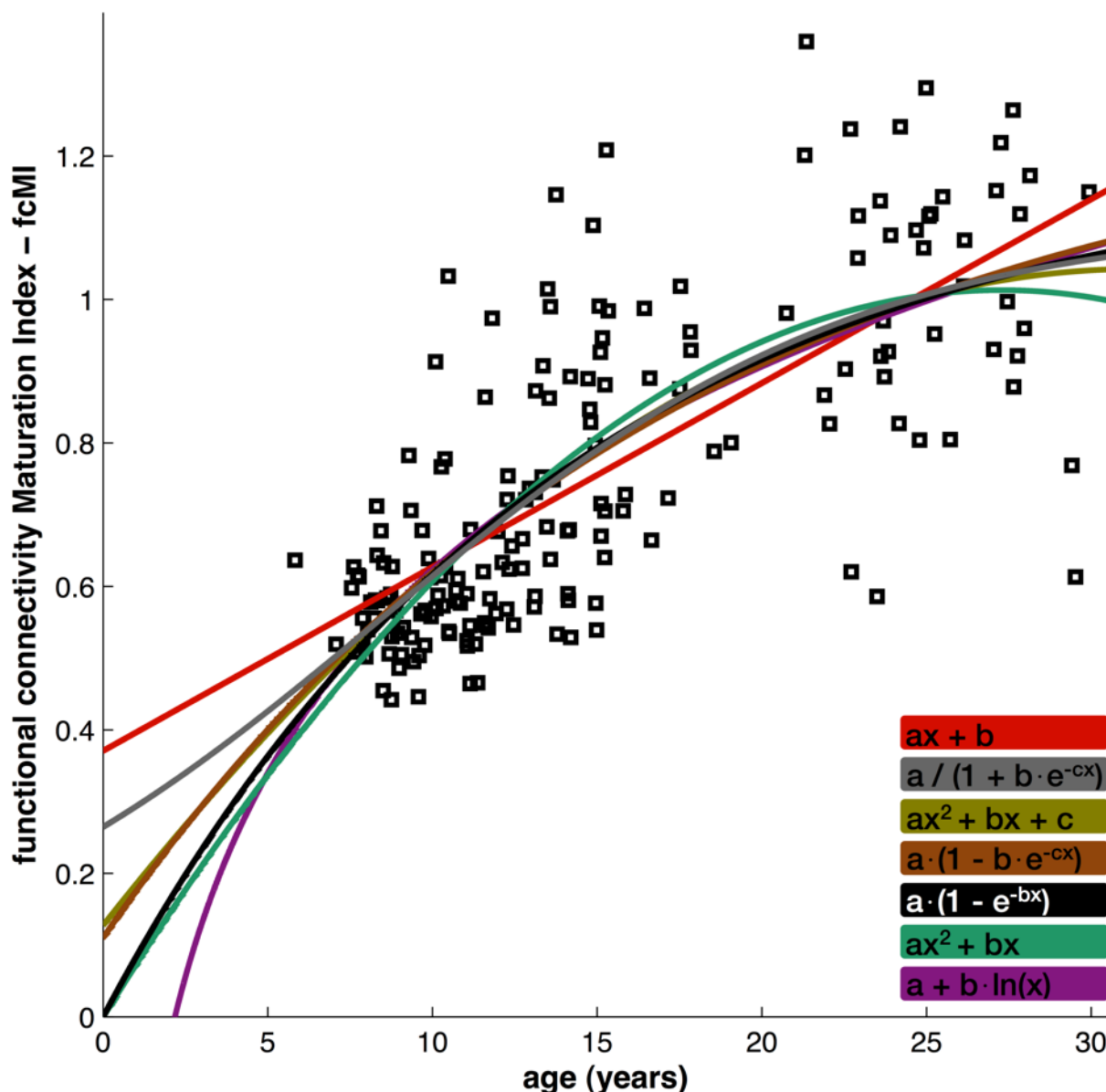


Fig. S4. Individual functional brain maturity levels (black squares) for data set 3. Chronological age is shown on the x-axis and the functional connectivity Maturation Index (fcMI) on the y-axis. Fitted curves for functions included in model selection are shown (linear – red; Pearl-Reed – gray; quadratic – green/brown; Von Bertalanffy with y-intercept – brown; Von Bertalanffy – black; quadratic constrained to origin – green; log – purple).

The brain maturity prediction results for data set 3 (Fig. S4, Table S4; four scans older than 30 years excluded from curve fits for consistency) were also very similar to the results from our other data sets. As for data set 1 and data set 2, linear provided the relatively worst fit (AIC weight ~ 0). All other models had relatively good fits with r^2 values of 0.55 and better. The best fit for data set 3 was provided by the Pearl-Reed growth curve (Table S4).

Combining fcMI measurements across data types

The similar brain maturity prediction results across disparate data sets (data set 1, 2 and 3) suggested that generating fcMI values for each data set separately, they could then be combined to generate a more precise maturation curve constrained by all available samples (Fig. S5, Fig. S6).

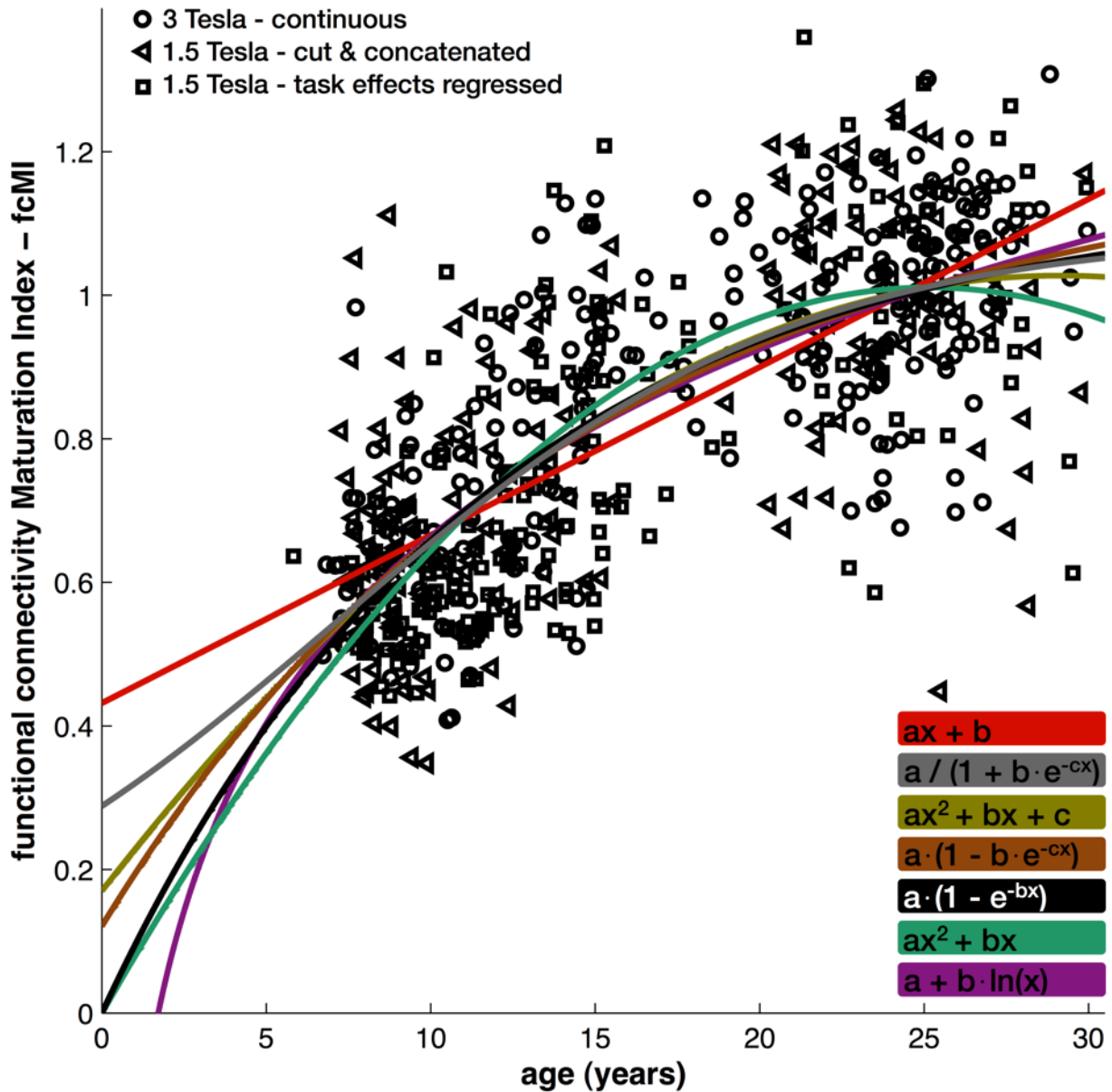


Fig. S5. Individual functional brain maturity levels combining data sets 1, 2, 3. Scans from data set 1 (continuous pure rest scans, 3Tesla) are indicated by circles, scans from data set 2 (cut & concatenated rest periods, 1.5 Tesla) are indicated by triangles, scans from data set 3 (event-related fMRI, task-effects regressed out, 1.5 Tesla) are indicated by squares. Chronological age is shown on the x-axis and the functional connectivity Maturation Index (fcMI) on the y-axis. Fitted curves for functions included in model selection are shown (linear – red; Pearl-Reed – gray; quadratic – green/brown; Von Bertalanffy with y-intercept – brown; Von Bertalanffy – black; quadratic constrained to origin – green; log – purple).

The Pearl-Reed growth function best fit the combined datasets between ages 6-30 years (Fig. S5, Fig. S6, Table S4). The linear fit was very poor with an ΔAIC of 29 and an AIC weight

of zero. The log and quadratic constrained to the origin also provided relatively poor fits with ΔAICs of around 10 and AIC weights close to zero.

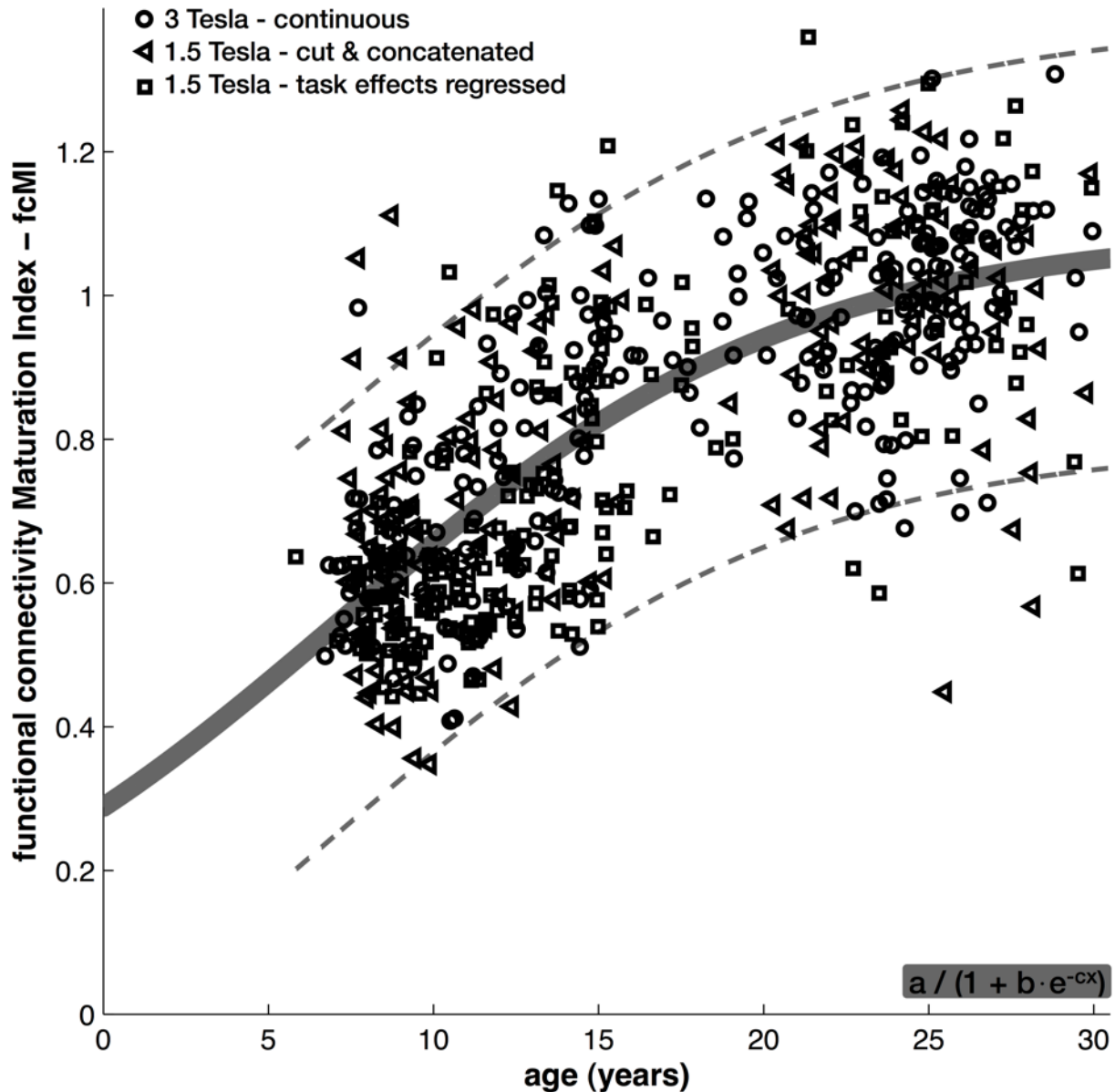


Fig. S6. Functional maturation curve for combined data. Individual functional brain maturity levels combining data sets 1, 2, 3. Scans from data set 1 (continuous pure rest scans, 3Tesla) are indicated by circles, scans from data set 2 (cut & concatenated rest periods, 1.5 Tesla) are indicated by triangles, scans from data set 3 (event-related fMRI, task-effects regressed out, 1.5 Tesla) are indicated by squares. Chronological age is shown on the x-axis and the functional connectivity Maturation Index (fcMI) on the y-axis. Functional connectivity maturation with best fit (Pearl-Reed) is shown by bold gray line, 95% predictions limits are shown with dashed gray lines.

The Pearl-Reed model predicts a non-zero fcMI (~0.3) at birth, and somewhat faster

maturity rates during puberty followed by an asymptotic plateau in young adulthood, all of which seem biologically plausible.

Significant differences between weakening and strengthening connections

Striking differences were observed between strengthening (positive correlation between connection strength and chronological age; orange) and weakening (negative correlation between connection strength and chronological age; light green) functional connections (Fig. S7, Fig. S8, Table S5).

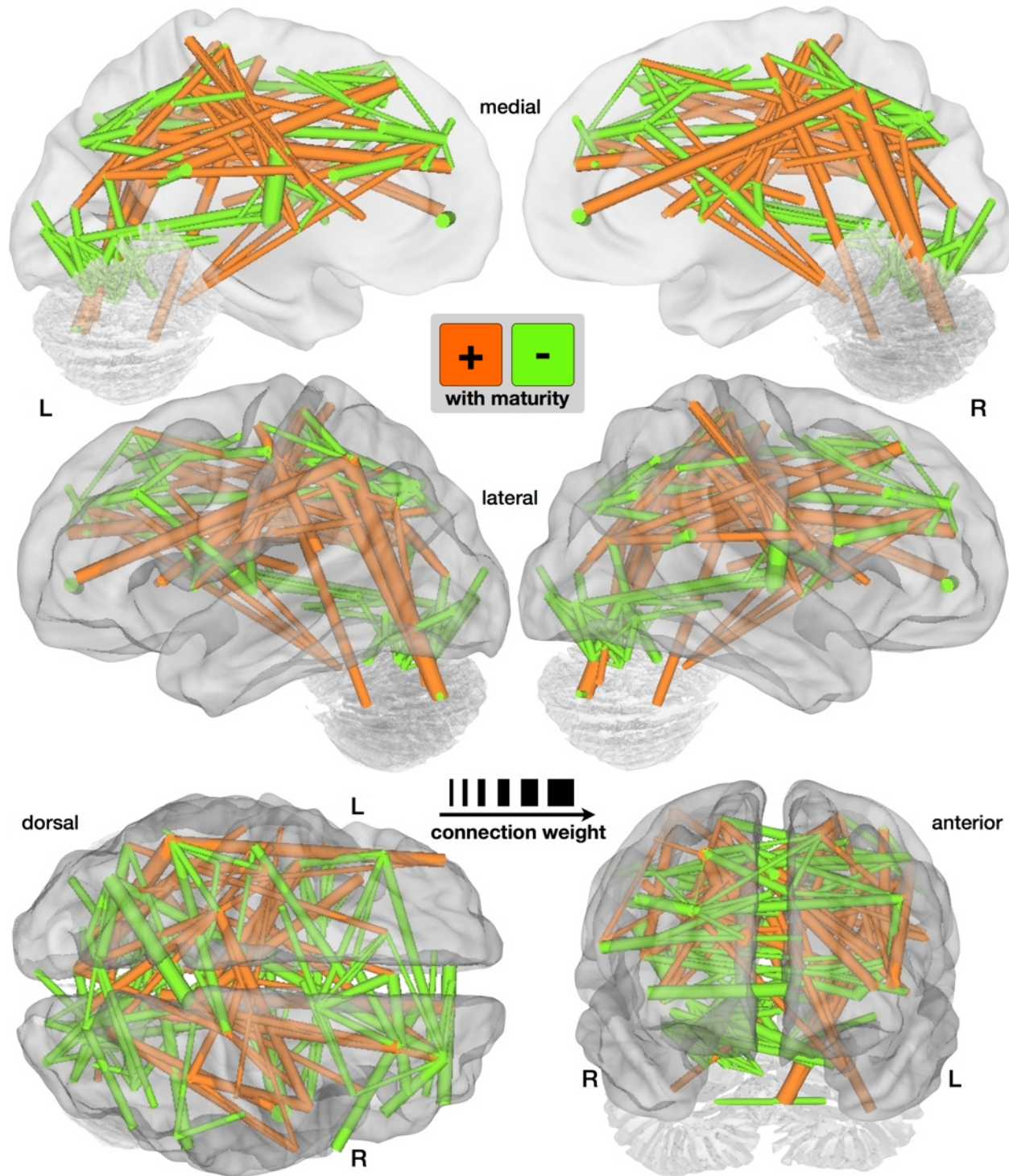


Fig. S7. Functional connectivity multivariate pattern analysis (fcMVPA) functional connection weights (feature weights). The functional connections driving the SVR brain maturity predictor are displayed on a surface rendering of the brain. The thickness of the 156 consensus functional connections scales with their weights. Connections positively correlated with age (stronger with increasing age) are shown in orange, whereas connections negatively correlated with age (weaker with increasing age) are shown in light green.

The functional connections that grew in strength with maturation were significantly ($t(154) = 14.66$, $P < 1 \times 10^{-30}$) longer in anatomical vector distance (mean length 80 mm) than the functional connections that diminished in strength (mean length 37 mm) (Fig. S7, Fig. S8). Growing-up functional connections were also significantly ($t(154) = 4.84$, $P < 1 \times 10^{-5}$) more likely to run along the anterior-posterior (AP) axis in the horizontal plane (mean angle 37 deg) than the growing-down functional connections (mean angle 58 deg) (Fig. S7, Fig. S8). No obvious differences between intra- and inter-hemispheric functional connections were noted (Fig. S8; filled vs. empty diamonds). Sixty-eight percent of the total connection weights were assigned to connections that weakened (light green), highlighting their great importance for predicting brain maturity.

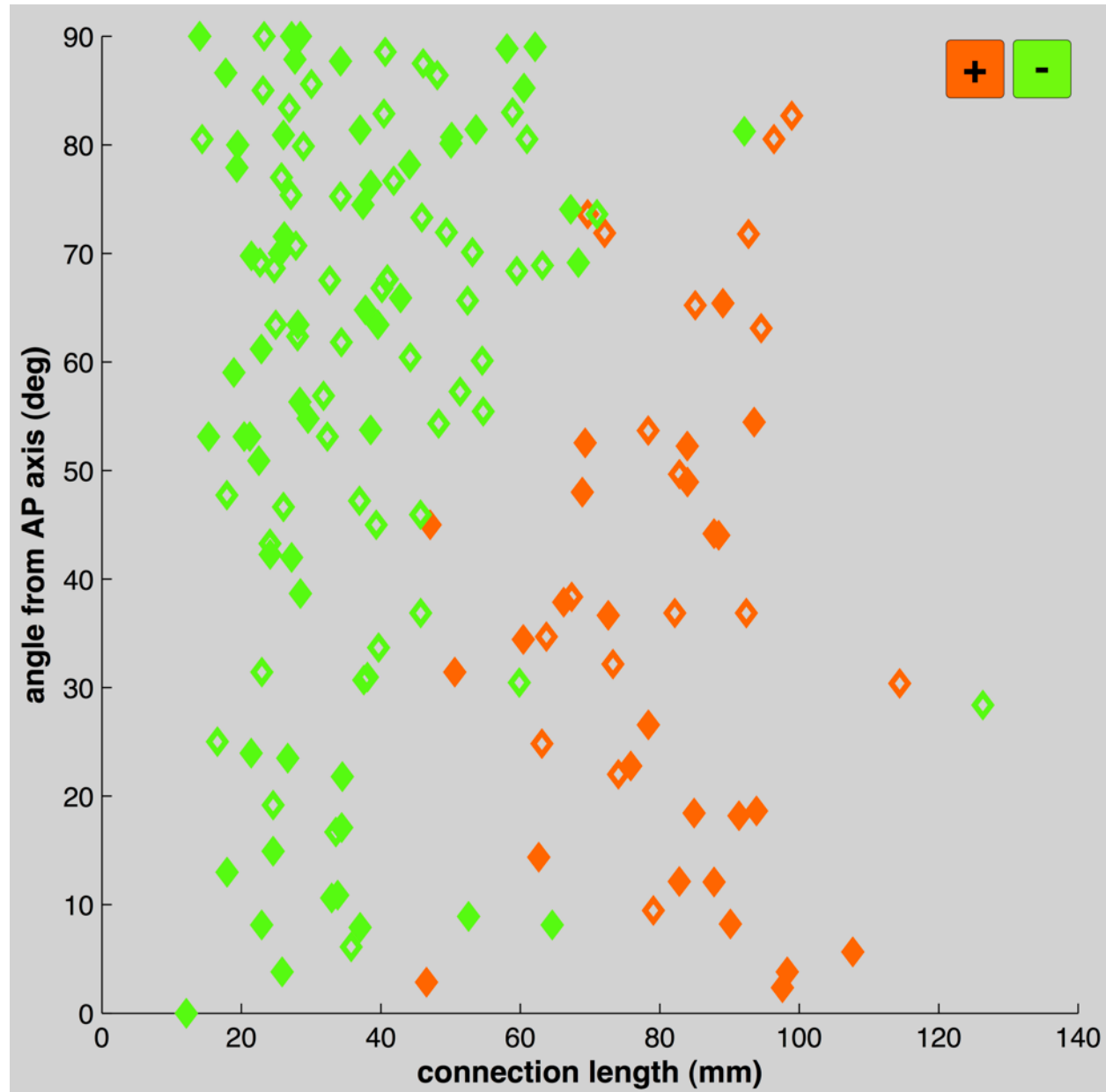


Fig. S8. Lengths and angles of consensus functional connections. Consensus functional

connections (diamonds) are displayed in orange if they are positively correlated with chronological age (stronger with age), they are displayed in light green if they are negatively correlated with chronological age (weaker with age). Displayed on the x-axis is the length of functional connections in mm. Displayed on the y-axis is the absolute angle (in degrees) functional connections make with the anterior-posterior (AP) axis in the horizontal plane. Filled diamonds represent cerebral and cerebellar interhemispheric connections, as well as ipsilateral connections between the cerebellum and cortex. Empty diamonds indicate connections within cerebral and cerebellar hemispheres as well as contralateral connections between the cerebellum and cerebrum.

As stated in the main body of the report, the quantitative nature of fcMVPA revealed that functional segregation (weakening of short-range functional connections) is a more powerful overall predictor of individual functional brain maturity than functional integration (strengthening of long-range functional connections). It is unknown to what extent progressive events (e.g. myelination, axon terminal arborization, synapse formation) and regressive events (e.g., axon collateral pruning, removal of axon terminal branching, synaptic pruning) in neurogenesis (64), whether experience dependent or experience expectant (65), contribute to the functional connectivity changes observed here. (14, 66, 67). Although pure speculation, it seems plausible that functional segregation is related to progressive events (particularly pruning of synapses and exuberant axon terminals/collaterals), while functional integration has a closer relationship to myelination (68).

Patterns of predictor regions (nodes)

ROI or node weights were computed by equally dividing the weight assigned to each functional connection between its two constituent ROIs and then, summing all the assigned weights for each ROI (Fig. S9, Table S6).

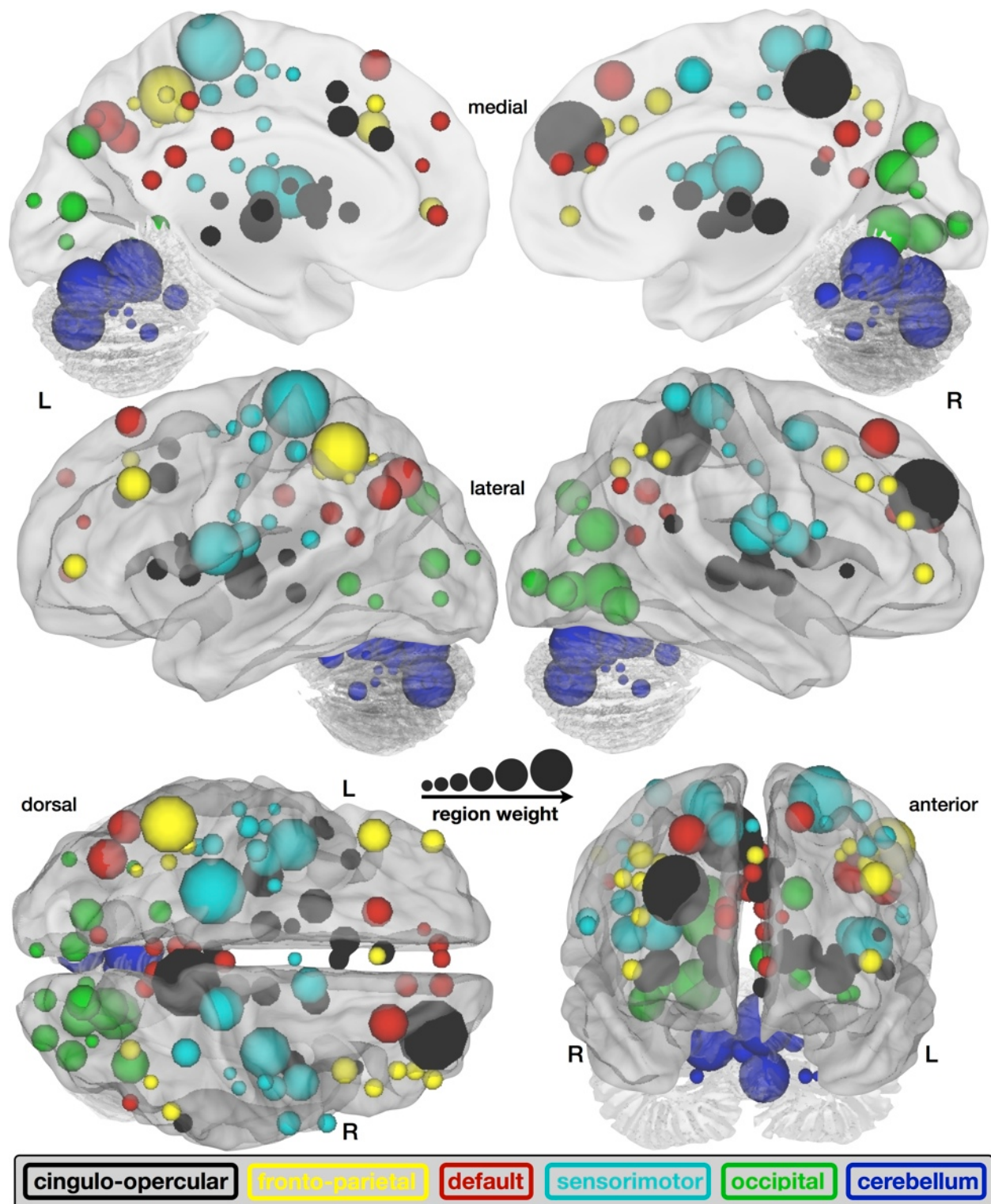


Fig. S9. Functional connectivity multivariate pattern analysis (fcMVPA) region (node) weights. All regions of interest (ROIs) that contributed to any of the 156 consensus functional connections are displayed, scaled by their node weights (1/2 sum of the weights of all the connections to and from that ROI). The ROIs are color-coded according to the six identified adult rs-fcMRI

networks (cingulo-opercular = black, fronto-parietal = yellow, default = red, sensorimotor = cyan, occipital = green, cerebellum = dark blue).

The ROI with the greatest relative prediction power about brain maturity was in right anterior prefrontal cortex (MNI coordinates: 27, 49, 26; shown in black Fig. 2, Fig. S9), thought to be important for cognitive control and higher-order relational reasoning (19, 69-71). This is consistent with developmental fMRI studies that have suggested that the activation profile of prefrontal cortex matures later in childhood and adolescence (2, 69-71).

The precuneus, which has recently been found to be most highly structurally (18) and functionally (72) connected, contained the second most predictive ROI (MNI coordinates: 8, -40, 50; shown in black Fig. 2, Fig. S9). It stands to reason that regions such as those in the precuneus, situated at the center of the adult brain's connectome could carry much information about how the network develops.

Supporting Tables

Table S1. Data sets available for analyses.

Data set	Tesla	data type	function	# frames	length	# scans	# females	# scans < 30 yrs
1	3 T	continuous rest	primary	126	~ 5 min	238	115	238
2	1.5 T	cut & concatenated rest	confirmatory	128	~ 5 min	195	101	193
3	1.5 T	event-related; task effects regressed	confirmatory	128	~ 5 min	186	99	182
all	-	-	-	-	-	619	315	613

Table S2. Subject demographics.

Data set 1

age (years)			# of subjects			IQ (est.)	
bin	mean	range	total	F	M	mean	range
<10	8.5	6.7-9.9	39	20	19	120.0	86-141
10-13	11.9	10.1-13.8	44	9	35	117.4	89-141
14-17	15.2	14.1-17.8	31	14	17	110.9	86-131
18-21	20.4	18.1-21.9	28	17	11	---	---
22-25	24.3	22.1-25.9	63	37	26	---	---
26-29	27.2	26.1-29.9	33	18	15	---	---
> 30	---	---	0	0	0	---	---

Data set 2

age (years)			# of subjects			IQ (est.)	
bin	mean	range	total	F	M	mean	range
<10	8.6	7-9.9	62	35	27	115.2	84-131
10-13	12.1	10.5-13.8	37	17	20	111.3	89-137
14-17	15.0	14.1-15.7	11	3	8	103.0	94-124
18-21	21.1	19-21.9	22	15	7	---	---
22-25	23.9	22-25.7	45	23	22	---	---
26-39	27.7	26-29.9	16	6	10	---	---
> 30	30.8	30.2-31.4	2	2	0	---	---

Data set 3

age (years)			# of subjects			IQ (est.)	
bin	mean	range	total	F	M	mean	range
<10	8.7	5.8-9.9	47	24	23	118.4	98-156
10-13	11.9	10.1-13.8	57	32	25	118.5	98-156
14-17	15.5	14.1-17.8	33	17	16	116.2	96-128
18-21	20.5	18.6-21.9	6	4	2	---	---
22-25	24.0	22.1-25.7	24	11	13	---	---
26-39	27.8	26.1-29.9	15	8	7	---	---
> 30	32.1	30.3-35.3	4	3	1	---	---

All data

age (years)			# of subjects			IQ (est.)	
bin	mean	range	total	F	M	mean	range
<10	8.6	5.8-9.9	148	79	69	117.5	84-156
10-13	11.9	10.1-13.8	138	58	80	116.2	89-156
14-17	15.3	14.1-17.8	75	34	41	111.9	86-131
18-21	20.7	18.1-21.9	56	36	20	---	---
22-25	24.1	22.1-25.9	132	71	61	---	---
26-29	27.5	26.1-29.9	64	32	32	---	---
> 30	31.7	30.2-35.3	6	5	1	---	---

Table S3. Meta-analyses of fMRI studies used for region of interest definition.

meta-analysis	# of studies	# subjects	Z-score threshold
Sensorimotor	12	310	7
Language	14	336	7
Default-mode	11	217	7 (trials); 2 (sustained)
Error-related	8	176	4
Memory	5	128	2

Table S4. Model selection and curve fitting.

Data set	data type	function	equation	r ²	adj. r ²	Δ AIC	w(AIC)	parameter		
								a	b	c
1	3T - continuous rest	Von Bertalanffy	a · (1 - e ^{-bx})	0.553	0.551	0.00	0.30	1.11	0.10	-
		Pearl-Reed	a / (1 + b · e ^{-cx})	0.555	0.552	0.57	0.23	1.07	2.55	0.15
		Log	a + b · ln(x)	0.551	0.549	0.76	0.21	-0.11	0.35	-
		Von Bertalanffy (y-intercept)	a · (1 - b · e ^{-cx})	0.554	0.550	1.53	0.14	1.15	0.90	0.08
		Quadratic	ax ² + bx + c	0.553	0.549	1.95	0.11	-0.00	0.05	0.26
		Quadratic (constr. to origin)	ax ² + bx	0.531	0.529	11.52	0.00	-0.00	0.08	-
		Linear	ax + b	0.532	0.530	10.95	0.00	0.02	0.49	-
2	1.5T – cut & concatenated rest	Von Bertalanffy	a · (1 - e ^{-bx})	0.511	0.509	3.29	0.08	1.11	0.09	-
		Pearl-Reed	a / (1 + b · e ^{-cx})	0.519	0.514	2.37	0.12	1.07	2.70	0.15
		Log	a + b · ln(x)	0.506	0.504	5.37	0.03	-0.15	0.36	-
		Von Bertalanffy (y-intercept)	a · (1 - b · e ^{-cx})	0.512	0.507	5.04	0.03	1.15	0.92	0.08
		Quadratic	ax ² + bx + c	0.524	0.519	0.32	0.34	-0.00	0.07	0.12
		Quadratic (constr. to origin)	ax ² + bx	0.520	0.517	0.00	0.40	-0.00	0.08	-
		Linear	ax + b	0.489	0.487	11.86	0.00	0.02	0.45	-
3	1.5T - event-rel; task regressed out	Von Bertalanffy	a · (1 - e ^{-bx})	0.554	0.552	1.07	0.17	1.20	0.07	-
		Pearl-Reed	a / (1 + b · e ^{-cx})	0.562	0.557	0.00	0.29	1.11	3.20	0.14
		Log	a + b · ln(x)	0.550	0.548	2.82	0.07	-0.32	0.41	-
		Von Bertalanffy (y-intercept)	a · (1 - b · e ^{-cx})	0.556	0.551	2.50	0.08	1.29	0.91	0.06
		Quadratic	ax ² + bx + c	0.560	0.555	0.74	0.20	-0.00	0.06	0.13
		Quadratic (constr. to origin)	ax ² + bx	0.555	0.553	0.82	0.19	-0.00	0.07	-
		Linear	ax + b	0.540	0.537	7.01	0.01	0.03	0.37	-
123	all	Von Bertalanffy	a · (1 - e ^{-bx})	0.551	0.550	6.30	0.02	1.14	0.09	-
		Pearl-Reed	a / (1 + b · e ^{-cx})	0.557	0.555	0.00	0.53	1.09	2.78	0.14
		Log	a + b · ln(x)	0.548	0.547	10.23	0.00	-0.20	0.38	-
		Von Bertalanffy (y-intercept)	a · (1 - b · e ^{-cx})	0.552	0.551	6.65	0.02	1.20	0.90	0.07
		Quadratic	ax ² + bx + c	0.557	0.555	0.49	0.42	-0.00	0.06	0.17
		Quadratic (constr. to origin)	ax ² + bx	0.548	0.547	10.56	0.00	-0.00	0.08	-
		Linear	ax + b	0.533	0.533	29.75	0.00	0.02	0.43	-

Table S5. Consensus features (156 functional connections) for SVR brain maturity prediction, their correlation with chronological age and their feature weights, sorted by functional modules.

ROI A: MNI coordinates				ROI B: MNI coordinates							
x	y	z	ROI label A	x	y	z	ROI label B	network B	corr w/ age	weight	
32	-12	2	mid insula	cingulo-opercular	11	-24	2	basal ganglia	cingulo-opercular	-0.43	4.8
14	6	7	basal ganglia	cingulo-opercular	37	-2	-3	mid insula	cingulo-opercular	-0.35	3.9
-20	6	7	basal ganglia	cingulo-opercular	-48	6	1	vFC	cingulo-opercular	-0.36	6.0
-20	6	7	basal ganglia	cingulo-opercular	-46	10	14	vFC	cingulo-opercular	-0.36	4.1
-20	6	7	basal ganglia	cingulo-opercular	-36	18	2	ant insula	cingulo-opercular	-0.37	1.9
-30	-14	1	mid insula	cingulo-opercular	-12	-12	6	thalamus	cingulo-opercular	-0.35	6.1
11	-24	2	basal ganglia	cingulo-opercular	-12	-12	6	thalamus	cingulo-opercular	-0.36	8.5
11	-24	2	basal ganglia	cingulo-opercular	11	-12	6	thalamus	cingulo-opercular	-0.35	1.9
27	49	26	aPFC	cingulo-opercular	8	-40	50	precuneus	cingulo-opercular	0.36	6.2
27	49	26	aPFC	cingulo-opercular	-30	-28	9	post insula	cingulo-opercular	0.39	7.2
8	-40	50	precuneus	cingulo-opercular	37	-2	-3	mid insula	cingulo-opercular	0.37	5.0
8	-40	50	precuneus	cingulo-opercular	-48	6	1	vFC	cingulo-opercular	0.38	5.0
8	-40	50	precuneus	cingulo-opercular	-36	18	2	ant insula	cingulo-opercular	0.37	8.5
8	-40	50	precuneus	cingulo-opercular	38	21	-1	ant insula	cingulo-opercular	0.42	5.0
-2	30	27	ACC	cingulo-opercular	40	36	29	dIPFC	fronto-parietal	-0.35	9.1
27	49	26	aPFC	cingulo-opercular	40	17	40	dPFC	fronto-parietal	-0.37	3.1
27	49	26	aPFC	cingulo-opercular	-44	27	33	dIPFC	fronto-parietal	-0.36	7.5
27	49	26	aPFC	cingulo-opercular	46	28	31	dIPFC	fronto-parietal	-0.38	9.0
-6	17	34	basal ganglia	cingulo-opercular	-44	27	33	dIPFC	fronto-parietal	-0.38	3.8
58	-41	20	parietal	cingulo-opercular	-5	-52	17	post cingulate	default	-0.37	8.9
27	49	26	aPFC	cingulo-opercular	9	51	16	vmPFC	default	-0.35	3.6
27	49	26	aPFC	cingulo-opercular	0	51	32	mPFC	default	-0.37	3.1
27	49	26	aPFC	cingulo-opercular	-36	-69	40	IPS	default	-0.37	8.3
27	49	26	aPFC	cingulo-opercular	23	33	47	sup frontal	default	-0.41	0.2
27	49	26	aPFC	cingulo-opercular	-16	29	54	sup frontal	default	-0.36	3.0
8	-40	50	precuneus	cingulo-opercular	-36	-69	40	IPS	default	-0.40	12.2
8	-40	50	precuneus	cingulo-opercular	-48	-63	35	angular gyrus	default	-0.38	4.6
-6	17	34	basal ganglia	cingulo-opercular	23	33	47	sup frontal	default	-0.37	6.9
-6	17	34	basal ganglia	cingulo-opercular	-16	29	54	sup frontal	default	-0.43	4.1
0	15	45	mFC	cingulo-opercular	-16	29	54	sup frontal	default	-0.34	4.5
32	-12	2	mid insula	cingulo-opercular	33	-12	16	mid insula	sensorimotor	-0.47	6.7
32	-12	2	mid insula	cingulo-opercular	46	-8	24	precentral gyrus	sensorimotor	-0.34	14.9
14	6	7	basal ganglia	cingulo-opercular	43	1	12	vFC	sensorimotor	-0.36	5.2
14	6	7	basal ganglia	cingulo-opercular	33	-12	16	mid insula	sensorimotor	-0.36	4.7
14	6	7	basal ganglia	cingulo-opercular	-42	-3	11	mid insula	sensorimotor	-0.36	4.4
-20	6	7	basal ganglia	cingulo-opercular	43	1	12	vFC	sensorimotor	-0.38	4.2
-20	6	7	basal ganglia	cingulo-opercular	-36	-12	15	mid insula	sensorimotor	-0.40	2.4
-20	6	7	basal ganglia	cingulo-opercular	-42	-3	11	mid insula	sensorimotor	-0.47	5.3
-30	-14	1	mid insula	cingulo-opercular	33	-12	16	mid insula	sensorimotor	-0.37	7.1
-30	-14	1	mid insula	cingulo-opercular	-36	-12	15	mid insula	sensorimotor	-0.46	7.0
-30	-14	1	mid insula	cingulo-opercular	-42	-3	11	mid insula	sensorimotor	-0.42	9.7
37	-2	-3	mid insula	cingulo-opercular	-24	-30	64	parietal	sensorimotor	0.39	3.4
-12	-3	13	thalamus	cingulo-opercular	33	-12	16	mid insula	sensorimotor	-0.41	3.2
-12	-3	13	thalamus	cingulo-opercular	-36	-12	15	mid insula	sensorimotor	-0.39	3.4
11	-24	2	basal ganglia	cingulo-opercular	33	-12	16	mid insula	sensorimotor	-0.36	3.4
0	15	45	mFC	cingulo-opercular	-47	-18	50	parietal	sensorimotor	-0.37	7.3
8	-40	50	precuneus	cingulo-opercular	-42	-3	11	mid insula	sensorimotor	0.39	8.4
37	-2	-3	mid insula	cingulo-opercular	18	-27	62	parietal	sensorimotor	0.37	4.2
11	-12	6	thalamus	cingulo-opercular	33	-12	16	mid insula	sensorimotor	-0.37	3.7
-4	-31	-4	post cingulate	cingulo-opercular	19	-66	-1	occipital	occipital	-0.36	4.4
-12	-12	6	thalamus	cingulo-opercular	19	-66	-1	occipital	occipital	-0.40	3.1
11	-12	6	thalamus	cingulo-opercular	19	-66	-1	occipital	occipital	-0.45	5.6
11	-24	2	basal ganglia	cingulo-opercular	-18	-50	1	occipital	occipital	-0.35	5.9
-4	-31	-4	post cingulate	cingulo-opercular	36	-60	-8	occipital	occipital	-0.38	5.0
11	-12	6	thalamus	cingulo-opercular	20	-78	-2	occipital	occipital	-0.35	6.2
-12	-12	6	thalamus	cingulo-opercular	-18	-50	1	occipital	occipital	-0.35	2.4
11	-12	6	thalamus	cingulo-opercular	-18	-50	1	occipital	occipital	-0.38	1.1
-2	30	27	ACC	cingulo-opercular	-28	-44	-25	lat cerebellum	cerebellum	0.37	5.2

ROI A: MNI coordinates				ROI B: MNI coordinates				corr w/ age	weight
x	y	z	ROI label A	x	y	z	ROI label B		
27	49	26	aPFC	-28	-44	-25	lat cerebellum	cerebellum	0.37
-6	17	34	basal ganglia	-28	-44	-25	lat cerebellum	cerebellum	0.37
-48	-47	49	IPL	-43	47	2	vent aPFC	fronto-parietal	0.41
-43	47	2	vent aPFC	-32	-58	46	IPS	fronto-parietal	0.37
42	48	-3	vent aPFC	-6	50	-1	vmPFC	default	-0.36
39	42	16	vIPFC	0	51	32	mPFC	default	-0.36
39	42	16	vIPFC	-11	45	17	vmPFC	default	-0.36
-48	-47	49	IPL	-24	-30	64	parietal	sensorimotor	-0.40
-1	28	40	ACC	10	5	51	pre-SMA	sensorimotor	-0.37
-48	-47	49	IPL	-38	-15	59	parietal	sensorimotor	-0.37
-48	-47	49	IPL	18	-27	62	parietal	sensorimotor	-0.40
-48	-47	49	IPL	-41	-31	48	post parietal	sensorimotor	-0.40
40	17	40	dFC	-26	-8	54	parietal	sensorimotor	-0.35
40	17	40	dFC	10	5	51	pre-SMA	sensorimotor	-0.39
40	17	40	dFC	0	-1	52	SMA	sensorimotor	-0.35
54	-44	43	IPL	46	-20	45	parietal	sensorimotor	-0.36
-44	27	33	dIPFC	10	5	51	pre-SMA	sensorimotor	-0.36
-44	27	33	dIPFC	-42	-3	11	mid insula	sensorimotor	-0.35
54	-44	43	IPL	-41	-31	48	post parietal	sensorimotor	-0.35
-53	-50	39	IPL	-41	-31	48	post parietal	sensorimotor	-0.43
44	-52	47	IPL	-16	-76	33	occipital	occipital	-0.35
32	-59	41	IPS	-16	-76	33	occipital	occipital	-0.38
32	-59	41	IPS	29	-73	29	occipital	occipital	-0.36
-35	-46	48	post parietal	-6	-79	-33	inf cerebellum	cerebellum	0.35
-48	-47	49	IPL	-6	-79	-33	inf cerebellum	cerebellum	0.38
-41	-40	42	IPL	-6	-79	-33	inf cerebellum	cerebellum	0.35
9	51	16	vmPFC	5	-50	33	precuneus	default	0.36
9	39	20	ACC	-5	-43	25	post cingulate	default	0.38
-9	-72	41	occipital	-48	-63	35	angular gyrus	default	-0.35
-48	-63	35	angular gyrus	-16	29	54	sup frontal	default	0.37
10	-55	17	post cingulate	23	33	47	sup frontal	default	0.39
23	33	47	sup frontal	5	-50	33	precuneus	default	0.35
-3	-38	45	precuneus	-24	-30	64	parietal	sensorimotor	-0.36
9	39	20	ACC	58	11	14	frontal	sensorimotor	-0.35
1	-26	31	post cingulate	-47	-18	50	parietal	sensorimotor	-0.36
-3	-38	45	precuneus	18	-27	62	parietal	sensorimotor	-0.41
23	33	47	sup frontal	10	5	51	pre-SMA	sensorimotor	-0.35
-16	29	54	sup frontal	10	5	51	pre-SMA	sensorimotor	-0.35
-36	-69	40	IPS	-16	-76	33	occipital	occipital	-0.43
9	-43	25	precuneus	15	-77	32	occipital	occipital	-0.36
-5	-43	25	post cingulate	15	-77	32	occipital	occipital	-0.36
-36	-69	40	IPS	15	-77	32	occipital	occipital	-0.36
51	-59	34	angular gyrus	15	-77	32	occipital	occipital	-0.34
1	-26	31	post cingulate	-37	-54	-37	inf cerebellum	cerebellum	0.34
-48	-63	35	angular gyrus	33	-73	-30	inf cerebellum	cerebellum	0.35
-54	-9	23	precentral gyrus	41	-23	55	parietal	sensorimotor	0.37
58	-3	17	precentral gyrus	-24	-30	64	parietal	sensorimotor	0.36
58	-3	17	precentral gyrus	34	-39	65	sup parietal	sensorimotor	0.36
-24	-30	64	parietal	43	1	12	vFC	sensorimotor	0.38
-24	-30	64	parietal	33	-12	16	mid insula	sensorimotor	0.38
-24	-30	64	parietal	-36	-12	15	mid insula	sensorimotor	0.36
-41	-37	16	temporal	-38	-15	59	parietal	sensorimotor	0.36
34	-39	65	sup parietal	43	1	12	vFC	sensorimotor	0.39
34	-39	65	sup parietal	-42	-3	11	mid insula	sensorimotor	0.37
18	-27	62	parietal	33	-12	16	mid insula	sensorimotor	0.37
18	-27	62	parietal	-36	-12	15	mid insula	sensorimotor	0.38
-24	-30	64	parietal	-5	-80	9	post occipital	occipital	0.35
18	-27	62	parietal	-5	-80	9	post occipital	occipital	0.35
-47	-12	36	parietal	17	-68	20	occipital	occipital	0.35
-24	-30	64	parietal	9	-76	14	occipital	occipital	0.36
-54	-22	22	precentral gyrus	-16	-76	33	occipital	occipital	0.35

ROI A: MNI coordinates				ROI B: MNI coordinates							
x	y	z	ROI label A	x	y	z	ROI label B	network B	corr w/ age	weight	
58	-3	17	precentral gyrus	sensorimotor	17	-68	20	occipital	occipital	0.36	6.9
-24	-30	64	parietal	sensorimotor	17	-68	20	occipital	occipital	0.37	5.0
-47	-18	50	parietal	sensorimotor	17	-68	20	occipital	occipital	0.36	1.4
44	-11	38	precentral gyrus	sensorimotor	17	-68	20	occipital	occipital	0.37	6.6
-5	-80	9	post occipital	occipital	14	-75	-21	med cerebellum	cerebellum	-0.41	6.7
33	-81	-2	post occipital	occipital	-16	-64	-21	med cerebellum	cerebellum	-0.36	5.9
33	-81	-2	post occipital	occipital	14	-75	-21	med cerebellum	cerebellum	-0.41	6.0
33	-81	-2	post occipital	occipital	1	-66	-24	med cerebellum	cerebellum	-0.36	3.4
33	-81	-2	post occipital	occipital	-6	-60	-15	med cerebellum	cerebellum	-0.38	5.1
-37	-83	-2	post occipital	occipital	-6	-60	-15	med cerebellum	cerebellum	-0.35	5.9
36	-60	-8	occipital	occipital	-24	-54	-21	lat cerebellum	cerebellum	-0.35	5.2
13	-91	2	post occipital	occipital	14	-75	-21	lat cerebellum	cerebellum	-0.38	5.0
20	-78	-2	occipital	occipital	1	-66	-24	lat cerebellum	cerebellum	-0.40	4.5
27	-91	2	post occipital	occipital	-6	-60	-15	lat cerebellum	cerebellum	-0.35	3.8
19	-66	-1	occipital	occipital	-24	-54	-21	lat cerebellum	cerebellum	-0.35	8.7
19	-66	-1	occipital	occipital	14	-75	-21	med cerebellum	cerebellum	-0.36	7.1
19	-66	-1	occipital	occipital	1	-66	-24	med cerebellum	cerebellum	-0.38	3.2
19	-66	-1	occipital	occipital	-6	-60	-15	med cerebellum	cerebellum	-0.43	6.4
20	-78	-2	occipital	occipital	14	-75	-21	med cerebellum	cerebellum	-0.39	5.8
36	-60	-8	occipital	occipital	-6	-60	-15	lat cerebellum	cerebellum	-0.35	6.0
36	-60	-8	occipital	occipital	14	-75	-21	med cerebellum	cerebellum	-0.35	3.1
36	-60	-8	occipital	occipital	1	-66	-24	med cerebellum	cerebellum	-0.34	3.3
36	-60	-8	occipital	occipital	-6	-60	-15	med cerebellum	cerebellum	-0.37	4.1
13	-91	2	post occipital	occipital	14	-75	-21	med cerebellum	cerebellum	-0.39	4.5
13	-91	2	post occipital	occipital	-6	-60	-15	med cerebellum	cerebellum	-0.38	3.4
20	-78	-2	occipital	occipital	-6	-60	-15	med cerebellum	cerebellum	-0.41	3.8
20	-78	-2	occipital	occipital	36	-60	-8	med cerebellum	cerebellum	-0.39	3.1
20	-78	-2	occipital	occipital	13	-91	2	med cerebellum	cerebellum	-0.44	4.5
27	-91	2	post occipital	occipital	20	-78	-2	med cerebellum	cerebellum	-0.37	7.6
27	-91	2	post occipital	occipital	27	-91	2	med cerebellum	cerebellum	-0.35	5.5
-4	-94	12	post occipital	occipital	20	-78	-2	med cerebellum	cerebellum	-0.38	5.6
17	-68	20	occipital	occipital	-4	-94	12	med cerebellum	cerebellum	-0.35	6.7
-18	-50	1	occipital	occipital	-18	-50	1	med cerebellum	cerebellum	-0.38	3.5
-34	-60	-5	occipital	occipital	-34	-60	-5	med cerebellum	cerebellum	-0.38	5.2
-6	-79	-33	inf cerebellum	cerebellum	18	-81	-33	inf cerebellum	cerebellum	-0.38	4.7
-6	-79	-33	inf cerebellum	cerebellum	-21	-79	-33	inf cerebellum	cerebellum	-0.39	5.0
14	-75	-21	med cerebellum	cerebellum	1	-66	-24	med cerebellum	cerebellum	-0.37	2.2

Table S6. Region strengths (sum of feature weights) for 160 ROIs sorted by MNI coordinates.

MNI-coordinates				summed feature weights			
x	y	z	ROI label	+ corr w/ age	- corr w/ age	all	network
6	64	3	vmPFC	0.0	0.0	0.0	default
29	57	18	aPFC	0.0	0.0	0.0	fronto-parietal
-29	57	10	aPFC	0.0	0.0	0.0	fronto-parietal
0	51	32	mPFC	0.0	8.6	8.6	default
-25	51	27	aPFC	0.0	0.0	0.0	default
9	51	16	vmPFC	10.5	3.6	14.2	default
-6	50	-1	vmPFC	0.0	10.3	10.3	default
27	49	26	aPFC	18.5	37.9	56.4	cingulo-opercular
42	48	-3	vent aPFC	0.0	10.3	10.3	fronto-parietal
-43	47	2	vent aPFC	13.7	0.0	13.7	fronto-parietal
-11	45	17	vmPFC	0.0	4.2	4.2	default
39	42	16	vIPFC	0.0	9.6	9.6	fronto-parietal
8	42	-5	vmPFC	0.0	0.0	0.0	default
9	39	20	ACC	4.2	8.8	13.0	default
46	39	-15	vIPFC	0.0	0.0	0.0	default
40	36	29	dIPFC	0.0	9.1	9.1	fronto-parietal
23	33	47	sup frontal	15.2	12.8	28.0	default
34	32	7	vPFC	0.0	0.0	0.0	cingulo-opercular
-2	30	27	ACC	5.2	9.1	14.2	cingulo-opercular
-16	29	54	sup frontal	4.9	14.6	19.5	default
-1	28	40	ACC	0.0	7.8	7.8	fronto-parietal
46	28	31	dIPFC	0.0	9.0	9.0	fronto-parietal
-52	28	17	vPFC	0.0	0.0	0.0	fronto-parietal
-44	27	33	dIPFC	0.0	22.8	22.8	fronto-parietal
51	23	8	vFC	0.0	0.0	0.0	cingulo-opercular
38	21	-1	ant insula	5.0	0.0	5.0	cingulo-opercular
9	20	34	dACC	0.0	0.0	0.0	cingulo-opercular
-36	18	2	ant insula	8.5	1.9	10.5	cingulo-opercular
40	17	40	dFC	0.0	16.2	16.2	fronto-parietal
-6	17	34	basal ganglia	4.4	14.8	19.3	cingulo-opercular
0	15	45	mFC	0.0	11.8	11.8	cingulo-opercular
58	11	14	frontal	0.0	8.8	8.8	sensorimotor
-46	10	14	vFC	0.0	4.1	4.1	cingulo-opercular
44	8	34	dFC	0.0	0.0	0.0	fronto-parietal
60	8	34	dFC	0.0	0.0	0.0	sensorimotor
-42	7	36	dFC	0.0	0.0	0.0	fronto-parietal
-55	7	23	vFC	0.0	0.0	0.0	sensorimotor
-20	6	7	basal ganglia	0.0	23.8	23.8	cingulo-opercular
14	6	7	basal ganglia	0.0	18.2	18.2	cingulo-opercular
-48	6	1	vFC	5.0	6.0	10.9	cingulo-opercular
10	5	51	pre-SMA	0.0	25.0	25.0	sensorimotor
43	1	12	vFC	16.6	9.4	25.9	sensorimotor
0	-1	52	SMA	0.0	4.3	4.3	sensorimotor
37	-2	-3	mid insula	12.6	3.9	16.5	cingulo-opercular
53	-3	32	frontal	0.0	0.0	0.0	sensorimotor
58	-3	17	precentral gyrus	13.8	0.0	13.8	sensorimotor
-12	-3	13	thalamus	0.0	6.6	6.6	cingulo-opercular
-42	-3	11	mid insula	14.6	25.7	40.3	sensorimotor
-44	-6	49	precentral gyrus	0.0	0.0	0.0	sensorimotor
-26	-8	54	parietal	0.0	5.2	5.2	sensorimotor
46	-8	24	precentral gyrus	0.0	14.9	14.9	sensorimotor
-54	-9	23	precentral gyrus	3.1	0.0	3.1	sensorimotor
44	-11	38	precentral gyrus	6.6	0.0	6.6	sensorimotor
-47	-12	36	parietal	5.1	0.0	5.1	sensorimotor
33	-12	16	mid insula	9.9	28.8	38.7	sensorimotor
-36	-12	15	mid insula	11.1	12.8	23.9	sensorimotor
-12	-12	6	thalamus	0.0	20.0	20.0	cingulo-opercular
11	-12	6	thalamus	0.0	18.5	18.5	cingulo-opercular
32	-12	2	mid insula	0.0	26.4	26.4	cingulo-opercular

MNI-coordinates				summed feature weights			
x	y	z	ROI label	+ corr w/ age	- corr w/ age	all	network
59	-13	8	temporal	0.0	0.0	0.0	sensorimotor
-30	-14	1	mid insula	0.0	29.9	29.9	cingulo-opercular
-38	-15	59	parietal	8.1	4.2	12.3	sensorimotor
52	-15	-13	inf temporal	0.0	0.0	0.0	default
-47	-18	50	parietal	1.4	11.0	12.4	sensorimotor
46	-20	45	parietal	0.0	4.9	4.9	sensorimotor
-55	-22	38	parietal	0.0	0.0	0.0	sensorimotor
-54	-22	22	precentral gyrus	5.5	0.0	5.5	sensorimotor
-54	-22	9	temporal	0.0	0.0	0.0	sensorimotor
41	-23	55	parietal	3.1	0.0	3.1	sensorimotor
42	-24	17	post insula	0.0	0.0	0.0	sensorimotor
11	-24	2	basal ganglia	0.0	24.5	24.5	cingulo-opercular
-59	-25	-15	inf temporal	0.0	0.0	0.0	default
1	-26	31	post cingulate	8.4	3.7	12.1	default
18	-27	62	parietal	20.7	12.2	33.0	sensorimotor
-38	-27	60	parietal	0.0	0.0	0.0	sensorimotor
-30	-28	9	post insula	7.2	0.0	7.2	cingulo-opercular
-24	-30	64	parietal	44.6	8.8	53.4	sensorimotor
51	-30	5	temporal	0.0	0.0	0.0	cingulo-opercular
-41	-31	48	post parietal	0.0	11.5	11.5	sensorimotor
-4	-31	-4	post cingulate	0.0	9.4	9.4	cingulo-opercular
54	-31	-18	fusiform	0.0	0.0	0.0	cingulo-opercular
-41	-37	16	temporal	8.1	0.0	8.1	sensorimotor
-53	-37	13	temporal	0.0	0.0	0.0	sensorimotor
28	-37	-15	fusiform	0.0	0.0	0.0	default
-3	-38	45	precuneus	0.0	8.1	8.1	default
34	-39	65	sup parietal	18.0	0.0	18.0	sensorimotor
8	-40	50	precuneus	38.2	16.7	54.9	cingulo-opercular
-41	-40	42	IPL	10.2	0.0	10.2	fronto-parietal
58	-41	20	parietal	0.0	8.9	8.9	cingulo-opercular
-8	-41	3	post cingulate	0.0	0.0	0.0	default
-61	-41	-2	inf temporal	0.0	0.0	0.0	default
-28	-42	-11	occipital	0.0	0.0	0.0	default
-5	-43	25	post cingulate	4.2	7.5	11.8	default
9	-43	25	precuneus	0.0	6.6	6.6	default
43	-43	8	temporal	0.0	0.0	0.0	cingulo-opercular
54	-44	43	IPL	0.0	8.9	8.9	fronto-parietal
-55	-44	30	parietal	0.0	0.0	0.0	cingulo-opercular
-28	-44	-25	lat cerebellum	14.7	0.0	14.7	cerebellum
-35	-46	48	post parietal	6.8	0.0	6.8	fronto-parietal
42	-46	21	sup temporal	0.0	0.0	0.0	cingulo-opercular
-48	-47	49	IPL	23.4	21.3	44.6	fronto-parietal
-41	-47	29	angular gyrus	0.0	0.0	0.0	cingulo-opercular
-59	-47	11	temporal	0.0	0.0	0.0	cingulo-opercular
-53	-50	39	IPL	0.0	3.4	3.4	fronto-parietal
5	-50	33	precuneus	15.6	0.0	15.6	default
-18	-50	1	occipital	0.0	12.9	12.9	occipital
44	-52	47	IPL	0.0	5.1	5.1	fronto-parietal
-5	-52	17	post cingulate	0.0	8.9	8.9	default
-24	-54	-21	lat cerebellum	0.0	14.7	14.7	cerebellum
-37	-54	-37	inf cerebellum	8.4	0.0	8.4	cerebellum
10	-55	17	post cingulate	10.1	0.0	10.1	default
-6	-56	29	precuneus	0.0	0.0	0.0	default
-34	-57	-24	lat cerebellum	0.0	0.0	0.0	cerebellum
-32	-58	46	IPS	3.8	0.0	3.8	fronto-parietal
-11	-58	17	post cingulate	0.0	0.0	0.0	default
32	-59	41	IPS	0.0	10.7	10.7	fronto-parietal
51	-59	34	angular gyrus	0.0	6.8	6.8	default
-34	-60	-5	occipital	0.0	5.2	5.2	occipital
36	-60	-8	occipital	0.0	26.7	26.7	occipital

MNI-coordinates				summed feature weights			
x	y	z	ROI label	+ corr w/ age	- corr w/ age	all	network
-6	-60	-15	med cerebellum	0.0	50.2	50.2	cerebellum
-25	-60	-34	inf cerebellum	0.0	0.0	0.0	cerebellum
32	-61	-31	inf cerebellum	0.0	0.0	0.0	cerebellum
46	-62	5	temporal	0.0	0.0	0.0	occipital
-48	-63	35	angular gyrus	10.4	12.7	23.1	default
-52	-63	15	TPJ	0.0	0.0	0.0	cingulo-opercular
-44	-63	-7	occipital	0.0	0.0	0.0	occipital
-16	-64	-21	med cerebellum	0.0	11.7	11.7	cerebellum
21	-64	-22	lat cerebellum	0.0	18.5	18.5	cerebellum
19	-66	-1	occipital	0.0	38.4	38.4	occipital
1	-66	-24	med cerebellum	0.0	15.2	15.2	cerebellum
-34	-67	-29	inf cerebellum	0.0	0.0	0.0	cerebellum
11	-68	42	precuneus	0.0	0.0	0.0	default
17	-68	20	occipital	24.9	6.7	31.6	occipital
-36	-69	40	IPS	0.0	28.9	28.9	default
39	-71	13	occipital	0.0	0.0	0.0	occipital
-9	-72	41	occipital	0.0	8.2	8.2	default
45	-72	29	occipital	0.0	0.0	0.0	default
-11	-72	-14	med cerebellum	0.0	0.0	0.0	cerebellum
29	-73	29	occipital	0.0	4.0	4.0	occipital
33	-73	-30	inf cerebellum	5.5	0.0	5.5	cerebellum
-2	-75	32	occipital	0.0	0.0	0.0	default
-29	-75	28	occipital	0.0	0.0	0.0	occipital
5	-75	-11	med cerebellum	0.0	0.0	0.0	cerebellum
14	-75	-21	med cerebellum	0.0	46.6	46.6	cerebellum
-16	-76	33	occipital	5.5	16.9	22.5	occipital
-42	-76	26	occipital	0.0	0.0	0.0	default
9	-76	14	occipital	7.7	0.0	7.7	occipital
15	-77	32	occipital	0.0	24.1	24.1	occipital
20	-78	-2	occipital	0.0	27.9	27.9	occipital
-21	-79	-33	inf cerebellum	0.0	5.0	5.0	cerebellum
-6	-79	-33	inf cerebellum	30.4	9.6	40.0	cerebellum
-5	-80	9	post occipital	12.3	6.7	19.0	occipital
29	-81	14	post occipital	0.0	0.0	0.0	occipital
33	-81	-2	post occipital	0.0	20.4	20.4	occipital
18	-81	-33	inf cerebellum	0.0	4.7	4.7	cerebellum
-37	-83	-2	post occipital	0.0	5.9	5.9	occipital
-29	-88	8	post occipital	0.0	0.0	0.0	occipital
13	-91	2	post occipital	0.0	12.9	12.9	occipital
27	-91	2	post occipital	0.0	16.8	16.8	occipital
-4	-94	12	post occipital	0.0	5.6	5.6	occipital

Supporting References

- S1. D. A. Fair *et al.*, Development of distinct control networks through segregation and integration. *Proc. Natl. Acad. Sci. U.S.A.* **104**, 13507 (2007).
- S2. B. L. Schlaggar *et al.*, Functional neuroanatomical differences between adults and school-age children in the processing of single words. *Science* **296**, 1476 (2002).
- S3. T. T. Brown *et al.*, Developmental changes in human cerebral functional organization for word generation. *Cereb. Cortex* **15**, 275 (2005).
- S4. D. A. Fair *et al.*, A method for using blocked and event-related fMRI data to study "resting state" functional connectivity. *Neuroimage* **35**, 396 (2007).
- S5. T. B. Jones *et al.*, Sources of group differences in functional connectivity: an investigation applied to autism spectrum disorder. *Neuroimage* **49**, 401 (2010).
- S6. J. P. Mugler, 3rd, J. R. Brookeman, Three-dimensional magnetization-prepared rapid gradient-echo imaging (3D MP RAGE). *Magn. Reson. Med.* **15**, 152 (1990).
- S7. F. M. Miezin, L. Maccotta, J. M. Ollinger, S. E. Petersen, R. L. Buckner, Characterizing the hemodynamic response: Effects of presentation rate, sampling procedure, and the possibility of ordering brain activity based on relative timing. *Neuroimage* **11**, 735 (2000).
- S8. J. Talairach, P. Tournoux, *Co-Planar Stereotaxic Atlas of the Human Brain*. (Thieme Medical Publishers, Inc., New York, 1988).
- S9. J. L. Lancaster *et al.*, A Modality-Independent Approach to Spatial Normalization of Tomographic Images of the Human Brain. *Hum. Brain Mapp.* **3**, 209 (1995).
- S10. A. Z. Snyder, in *Quantification of Brain Function Using PET*, R. Myer, V. J. Cunningham, D. L. Bailey, T. Jones, Eds. (Academic Press, San Diego, CA, 1996), pp. 131-137.
- S11. M. D. Fox *et al.*, The human brain is intrinsically organized into dynamic, anticorrelated functional networks. *Proc. Natl. Acad. Sci. U.S.A.* **102**, 9673 (2005).
- S12. M. D. Fox, M. Corbetta, A. Z. Snyder, J. L. Vincent, M. E. Raichle, Spontaneous neuronal activity distinguishes human dorsal and ventral attention systems. *Proc. Natl. Acad. Sci. U.S.A.* **103**, 10046 (2006).
- S13. N. U. F. Dosenbach *et al.*, Distinct brain networks for adaptive and stable task control in humans. *Proc. Natl. Acad. Sci. U.S.A.* **104**, 11073 (2007).
- S14. D. A. Fair *et al.*, Functional brain networks develop from a "local to distributed" organization. *PLoS Comput. Biol.* **5**, e1000381 (2009).
- S15. D. A. Fair *et al.*, The maturing architecture of the brain's default network. *Proc. Natl. Acad. Sci. U.S.A.* **105**, 4028 (2008).
- S16. C. T. Butts, Revisiting the Foundations of Network Analysis. *Science* **325**, 414 (2009).
- S17. A. Zalesky *et al.*, Whole-brain anatomical networks: Does the choice of nodes matter? *Neuroimage* **50**, 970 (2010).
- S18. P. Hagmann *et al.*, Mapping the structural core of human cerebral cortex. *PLoS Biol.* **6**, e159 (2008).
- S19. N. U. F. Dosenbach *et al.*, A core system for the implementation of task sets. *Neuron* **50**, 799 (2006).
- S20. N. U. F. Dosenbach, D. A. Fair, A. L. Cohen, B. L. Schlaggar, S. E. Petersen, A dual-networks architecture of top-down control. *Trends Cogn. Sci.* **12**, 99 (2008).

- S21. V. Naumovich Vapnik, *Statistical learning theory*. Computational learning theory (Wiley, New York, NY, 1998), vol. II.
- S22. B. Schölkopf, A. J. Smola, *Learning with kernels: support vector machines, regularization, optimization and beyond*. (MIT Press, Cambridge, Massachusetts, 2002).
- S23. A. Ben-Hur, C. S. Ong, S. Sonnenburg, B. Schölkopf, G. Rätsch, Support vector machines and kernels for computational biology. *PLoS Comput. Biol.* **4**, e1000173 (2008).
- S24. F. Hoeft *et al.*, Morphometric spatial patterns differentiating boys with fragile X syndrome, typically developing boys, and developmentally delayed boys aged 1 to 3 years. *Arch. Gen. Psychiatry* **65**, 1087 (2008).
- S25. S. Klöppel *et al.*, Accuracy of dementia diagnosis: a direct comparison between radiologists and a computerized method. *Brain* **131**, 2969 (2008).
- S26. B. Magnin *et al.*, Support vector machine-based classification of Alzheimer's disease from whole-brain anatomical MRI. *Neuroradiology* **51**, 73 (2009).
- S27. S. Klöppel *et al.*, Automatic detection of preclinical neurodegeneration: presymptomatic Huntington disease. *Neurology* **72**, 426 (2009).
- S28. C. Ecker *et al.*, Investigating the predictive value of whole-brain structural MR scans in autism: a pattern classification approach. *Neuroimage* **49**, 44 (2010).
- S29. E. Formisano, F. De Martino, M. Bonte, R. Goebel, "Who" is saying "what"? Brain-based decoding of human voice and speech. *Science* **322**, 970 (2008).
- S30. M. Esterman, Y. C. Chiu, B. J. Tamber-Rosenau, S. Yantis, Decoding cognitive control in human parietal cortex. *Proc. Natl. Acad. Sci. U.S.A.* **106**, 17974 (2009).
- S31. F. De Martino *et al.*, Combining multivariate voxel selection and support vector machines for mapping and classification of fMRI spatial patterns. *Neuroimage* **43**, 44 (2008).
- S32. F. Pereira, T. M. Mitchell, M. Botvinick, Machine learning classifiers and fMRI: a tutorial overview. *Neuroimage* **45**, S199 (2009).
- S33. S. Bray, C. Chang, F. Hoeft, Applications of multivariate pattern classification analyses in developmental neuroimaging of healthy and clinical populations. *Front. Hum. Neurosci.* **3**, 32 (2009).
- S34. F. Jäkel, B. Schölkopf, F. Wichmann, Does Cognitive Science Need Kernels? *Trends Cogn. Sci.* **13**, 381 (2009).
- S35. C. J. C. Burges, A tutorial on support vector machines for pattern recognition. *Data. Min. Knowl. Disc.* **2**, 121 (1998).
- S36. S. Gunn, "Support Vector Machines for Classification and Regression" (Department of Electronics and Computer Science University of Southampton, 1998).
- S37. T. Hastie, R. Tibshirani, J. Friedman, *The elements of statistical learning: data mining, inference, and prediction*. Springer Series in Statistics (Springer, New York, NY, 2001).
- S38. A. Smola, B. Schölkopf, A tutorial on support vector regression. *Statist. Comput.* **14**, 199 (2004).
- S39. D. Basak, S. Pal, D. Patranabis, Support Vector Regression. *Neural Information Processing—Letters and Reviews* **11**, 203 (2007).
- S40. C.-w. Hsu, C.-c. Chang, C.-j. Lin, "A Practical Guide to Support Vector Classification" (Department of Computer Science National Taiwan University, 2003).

- S41. H. Drucker, B. L. Kaufman, A. Smola, V. Vapnik, in *Advances in Neural Information Processing Systems*, M. C. Mozer, J. I. Jordan, T. Petsche, Eds. (MIT Press, Cambridge, Massachusetts, 1997), vol. 9, pp. 155-161.
- S42. R. Kohavi, in *International Joint Conference on Artificial Intelligence (IJCAI)*. (Morgan Kaufmann Publishers, Montreal, Canada, 1995), pp. 1137-1145.
- S43. T. M. Mitchell *et al.*, Predicting human brain activity associated with the meanings of nouns. *Science* **320**, 1191 (2008).
- S44. F. Pereira, Carnegie Mellon University (2007).
- S45. M. Esterman, B. J. Tamber-Rosenau, Y.-C. Chiu, S. Yantis, Avoiding non-independence in fMRI data analysis: Leave one subject out. *Neuroimage* **50**, 572 (2010).
- S46. A. Statnikov, C. F. Aliferis, I. Tsamardinos, D. Hardin, S. Levy, A comprehensive evaluation of multicategory classification methods for microarray gene expression cancer diagnosis. *Bioinformatics* **21**, 631 (2005).
- S47. P. Golland, B. Fischl, in *Information processing in medical imaging*, C. J. Taylor, J. A. Noble, Eds. (Springer, Berlin, 2003), vol. 2732, pp. 330-41.
- S48. H. Akaike, in *Second International Symposium on Inference Theory*, B. N. Petrov, F. Csaki, Eds. (Akademiai Kiado, Budapest, 1973), pp. 267-81.
- S49. K. P. Burnham, D. R. Anderson, *Model selection and multimodal inference: A practical information-theoretic approach*. (Springer-Verlag, New York, NY, 2002).
- S50. E. Wagenmakers, S. Farrell, AIC model selection using Akaike weights. *Psychon. Bull. Rev.* **11**, 192 (2004).
- S51. G. Glatting, P. Kletting, S. Reske, K. Hohl, C. Ring, Choosing the optimal fit function: comparison of the Akaike information criterion and the F-test. *Med. Phys.* **34**, 4285 (2007).
- S52. M. E. J. Newman, Modularity and community structure in networks. *Proc. Natl. Acad. Sci. U.S.A.* **103**, 8577 (2006).
- S53. B. Karrer, E. Levina, M. E. J. Newman, Robustness of community structure in networks. *Physical Review E* **77**, 46119 (2008).
- S54. M. Meilă, Comparing clusterings—an information based distance. *Journal of Multivariate Analysis* **98**, 873 (2007).
- S55. D. C. Van Essen *et al.*, An integrated software suite for surface-based analyses of cerebral cortex. *J. Am. Med. Inform. Assoc.* **8**, 443 (2001).
- S56. D. C. Van Essen, A Population-Average, Landmark- and Surface-based (PALS) Atlas of Human Cerebral Cortex. *Neuroimage* **28**, 635 (2005).
- S57. D. C. Van Essen, D. L. Dierker, Surface-based and probabilistic atlases of primate cerebral cortex. *Neuron* **56**, 209 (2007).
- S58. A. Tsouolaris, J. Wallace, Analysis of logistic growth models. *Math. Biosci.* **179**, 21 (2002).
- S59. L. Bertalanffy, Quantitative Laws in Metabolism and Growth. *Q. Rev. Biol.* **32**, 217 (1957).
- S60. R. Pearl, L. Reed, A further note on the mathematical theory of population growth. *Proc. Natl. Acad. Sci. U.S.A.* **8**, 365 (1922).
- S61. R. Pearl, L. Reed, Skew-growth curves. *Proc. Natl. Acad. Sci. U.S.A.* **11**, 16 (1925).

- S62. C. D. Smyser *et al.*, Longitudinal Analysis of Neural Network Development in Preterm Infants. *Cereb. Cortex*, (2010).
- S63. P. Fransson *et al.*, Resting-state networks in the infant brain. *Proc. Natl. Acad. Sci. U.S.A.* **104**, 15531 (2007).
- S64. W. M. Cowan, J. Fawcett, D. D. M. O'Leary, B. B. Stanfield, Regressive events in neurogenesis. *Science* **225**, 1258 (1984).
- S65. W. T. Greenough, J. E. Black, C. S. Wallace, Experience and brain development. *Child Dev.* **58**, 539 (1987).
- S66. K. Supekar, M. Musen, V. Menon, Development of large-scale functional brain networks in children. *PLoS Biol.* **7**, e1000157 (2009).
- S67. L. H. Somerville, B. J. Casey, Developmental neurobiology of cognitive control and motivational systems. *Curr. Opin. Neurobiol.* **20**, 236 (2010).
- S68. D. A. Fair, B. L. Schlaggar, in *Encyclopedia of Brain Development*, M. M. Haith, J. B. Benson, Eds. (Academic Press, San Diego, CA, 2008).
- S69. S. A. Bunge, N. M. Dudukovic, M. E. Thomason, C. J. Vaidya, J. D. E. Gabrieli, Immature frontal lobe contributions to cognitive control in children: evidence from fMRI. *Neuron* **33**, 301 (2002).
- S70. E. A. Crone, C. Wendelken, S. Donohue, L. van Leijenhorst, S. A. Bunge, Neurocognitive development of the ability to manipulate information in working memory. *Proc. Natl. Acad. Sci. U.S.A.* **103**, 9315 (2006).
- S71. K. Velanova, M. E. Wheeler, B. Luna, The maturation of task set-related activation supports late developmental improvements in inhibitory control. *J. Neurosci.* **29**, 12558 (2009).
- S72. D. Tomasi, N. D. Volkow, Functional connectivity density mapping. *Proc. Natl. Acad. Sci. U.S.A.* **107**, 9885 (2010).